Investigation techniques and physical aspects of the angle of repose of granular matter

Sacha Duverger, Vasileios Angelidakis, Sadegh Nadimi, Stefano Utili, Stéphane Bonelli, Pierre Philippe, Jérôme Duriez

Investigation techniques and physical aspects of the angle of repose of granular matter

Sacha Duverger[1], Vasileios Angelidakis[2,3], Sadegh Nadimi[2], Stefano Utili[2], Stéphane Bonelli[1], Pierre Philippe[1] and Jérôme Duriez[1*]

[1]INRAE, Aix Marseille Univ, RECOVER, Aix-en-Provence, France.
[2]School of Engineering, Newcastle University, Newcastle upon Tyne, United Kingdom.
[3]Institute for Multiscale Simulation, Friedrich-Alexander-Universität Erlangen-Nürnberg, Germany.

*Corresponding author(s). E-mail(s): jerome.duriez@inrae.fr;
Contributing authors: sacha.duverger@inrae.fr; vasileios.angelidakis@fau.de;
sadegh.nadimi-shahraki@newcastle.ac.uk; stefano.utili@newcastle.ac.uk;
stephane.bonelli@inrae.fr; pierre.philippe@inrae.fr;

Abstract

The repose of granular materials is investigated via two different Discrete Element Method (DEM) implementations in comparison with an experimental reference from a recently proposed benchmark setup. On a methodological standpoint, a rigorous measurement method of the angle of repose (AOR) is first proposed for plane-strain and axisymmetric conditions as encountered in the reference experiments. Additionally, two systematic procedures are designed in order to also determine the void ratio of the heap, as a fundamental property of granular matter possibly influencing the AOR. A physical discussion is then developed on the role of particle shape, considering the non-spherical nature of reference particles with a convexity value of $\boldsymbol{C = 0.954}$. Adoping non-convex multi-spheres aggregates (i.e. clumps), the first DEM modelling approach successfully predicts the AOR within a 8% tolerance. After a convex simplification that neglects local concavities, another approach based on potential particles underestimates to a greater extent the AOR, bringing it down from $\mathbf{35.95 \pm 0.88^\circ}$ to $\mathbf{31.26 \pm 0.95^\circ}$. For the loading setup(s) at hand, the AOR is eventually shown to bear no constitutive nature. It is for instance independent of initial void ratio but is still different than the critical friction angle. The latter may actually serve as a lower bound for the process-dependent AOR. These conclusions are drawn from a statistical analysis of a large set of results, accounting for the random nature of the microscopic arrangement in the studied process.

Keywords: Angle of repose; Discrete Element Method; Non-spherical particles

1 Introduction

Under loading, particulate matter strains in the form of a fluid-like flow as long as the applied load is high enough. Then, once loading no longer prevails against internal dissipation in terms of energy input, particulate matter comes at rest in a solid-like heap configuration, especially in the absence of cohesion or adhesion. The corresponding slope, expressed in terms of an angle of repose (AOR), rules the spatial extents of the deposit for a given matter quantity. The AOR is therefore of interest for countless applications involving particulate materials, for instance the design of industrial facilities for granular-conveying processes, or the prediction of the coverage of natural deposits after e.g. snow or rock avalanches. Several standardised measurement procedures have been proposed in the literature to measure the AOR of granular materials employing empirical and geometrical concepts [1, 2] but they unfortunately often lead to inconsistent results, as demonstrated in [3], and new measurement devices are still being proposed [4]. As such, an one-to-one correlation of the AOR to theoretically-established mechanical properties is not always demonstrated even though the AOR may be often considered as a material property, e.g. in [5] in geotechnics or in [6, 7] for the purpose of DEM calibration. A part of the complexity certainly stems from an influence of non-constitutive parameters such as the heap construction history [8] and possible geometrical effects [9, 10]. The latter comes in addition to the more natural influence of physical microscopic properties such as particle shape [11, 12] and contact friction [11, 9, 12], as well as mesoscopic ones, such as fabric [12]. Last, it should be noted that granular heaps may not systematically conform to a linear slope [13, 14] which may prevent one to define a single-valued AOR.

Following up on these previous works, the aim of the present manuscript is twofold. First, rigorous simulation and measurement methods are proposed in order to ease evergoing AOR studies. Second, with the help of these methods, an in-depth study is conducted in order to gain further insights on the AOR variations with respect to physical parameters. The present analysis combines the use of two Discrete Element Method (DEM) approaches and existing experimental results recently proposed by the Japanese Geotechnical Society (JGS) as part of a round robin series of tests [4, 15].

The remainder of the article is as follows. Section 2 first recalls the JGS reference experiments [4] and the two DEM formulations which are both executed within the YADE code [16] but differ in the way the exact shape of the grains is described. Section 3 then introduces new methods enhancing AOR studies, namely a systematic definition of the AOR value after detection of the

external slope and versatile measurement methods of the packing compacity (void ratio) of the heap since the latter is a fundamental property of granular matter. It also provides a discussion on computational aspects of the two DEM approaches used to simulate the same JGS experiments. Section 4 finally provides new insights on the role of some physical parameters on the AOR value, after conducting a large number of DEM simulations interpreted in a statistics fashion for the sake of robust conclusions.

2 Reference benchmark experiments and DEM formulations

2.1 Reference benchmark experiments

Measurements of AOR data have been recently proposed by the JGS as part of a round robin test organised within the activities of Technical Committee 105 (TC105: Geo-Mechanics from Micro to Macro) of the International Society for Soil Mechanics and Geotechnical Engineering (ISSMGE) [4] and will serve here as reference. In a first step, data only included an experimental characterization of the granular material at hand, together with properties of the two experimental setups used for AOR measurement, before that blind DEM predictions of the AOR values could be proposed by international participants to the round robin and compared with experimental values [15].

An artificial granular material was considered with non-spherical particles made of 3D-printing resin. Particles constituting the mono-dispersed material resemble a tetrahedral arrangement of four spheres clumped together (see Figure 1). Individual spheres have a radius of $r_s = 0.3101\,cm$, while each global particle is inscribed in a radius $r_{clump} = 0.5\,cm$.

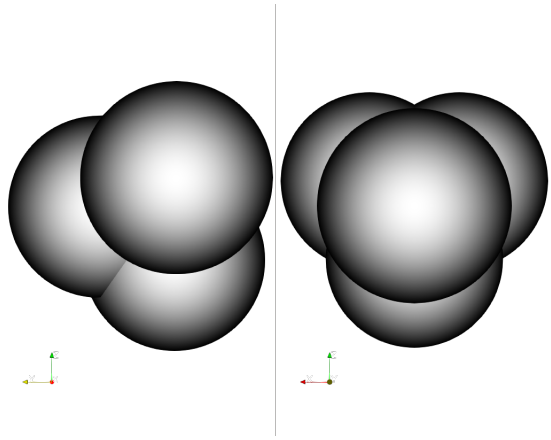

Fig. 1: Physical particle made of 4 clumped spheres.

The considered AOR setups consist of two devices in the form of either a cylindrical (see Figure 2) or cuboidal (see Figure 3) container with acrylic walls, aiming to compare how the AOR varies for heaps of different geometries. For the cylindrical case forming an axisymmetric configuration, the container encloses the particles before the surrounding wall is lowered until a small,

final, height of 1 cm. For the second device corresponding to a plane-strain configuration of the repose state, the cuboidal box encloses the particles initially, until one of the side walls is removed upwards, leaving eventually only a fixed 0.5 cm ridge to retain the lowest particles on that side. The reference number of particles, walls' velocity and boxes' dimensions are given in Table 1 for both configurations, as per the specifications of the round robin test. These parameters were also set to different values for some series of simulations in this study, see Section 4.5 for what concerns the number of particles and boxes' dimensions or Appendix C for the walls' velocity.

2.2 DEM shape description with clump and potential particles approaches

2.2.1 Clumps of spheres

In line with the physical particles at hand (see Figure 1), a first DEM approach adopts the traditional multi-sphere technique to simulate non-spherical particles. A rigid agglomeration of four spheres is created to reflect the particle morphology as a so-called clump, e.g. as shown in [17]. This technique leads to an increased total number of discrete elements in a simulation, compared to the number of physical particles, however it benefits from the low computational cost of collision detection among spheres. To define the inertial properties of a clump, many DEM codes still simply add the masses of the clump members and directly combine their inertia matrices, which leads to an overestimation in the case of clumps with overlapping members, like the one adopted to simulate the present 3D-printed particle. To mitigate this issue, methods to adjust the density of each sphere-member have been proposed in the literature, such as the one of Ferellec and McDowell [18] to correct mass and inertia at the cost of some pre-processing efforts. YADE, along with PFC, provide an alternative solution, where a three-dimensional grid of voxels is generated in the bounding box of the particle, and it is evaluated for each voxel whether it belongs to at least one sphere-member of the clump. For the particles at hand in this study, a grid size of $1000 \times 1000 \times 1000$ voxels is used to estimate the volume (and thus the mass) and inertia tensor, with negligible discretisation error induced by the grid resolution, since finer grids led to the same inertial properties.

2.2.2 Potential particles

While the above clump approach is a straightforward DEM strategy for describing the physical particles at hand (Figure 1), a comparison is carried out with a second approach using the so-called "potential particles" introduced by Houlsby [19], and extended to three-dimensions by Boon et al. [20]. The potential particles are generalised convex

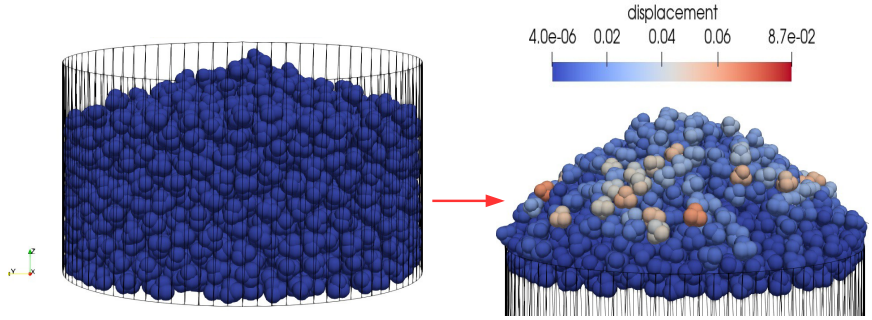

Fig. 2: Initial (left) and final (right) states of the heap in the axisymmetric configuration.

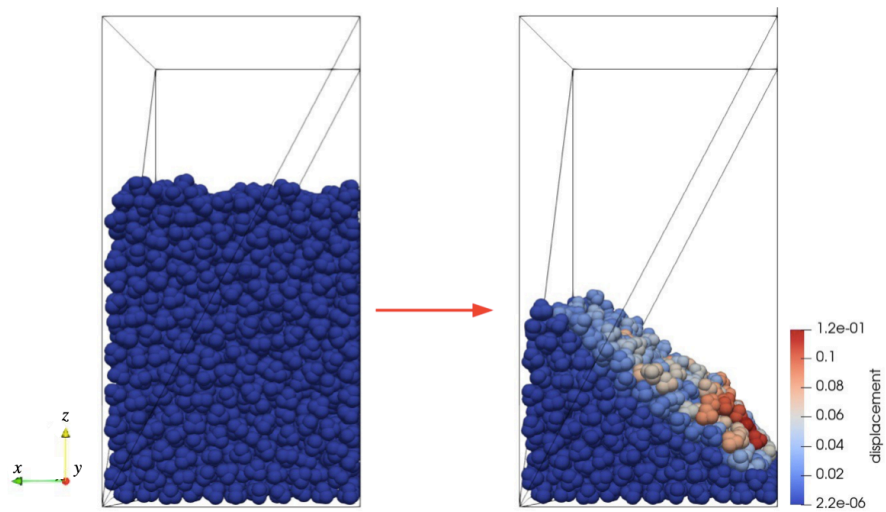

Fig. 3: Initial (left) and final (right) state of the heap in the plane strain configuration.

non-spherical particles, assembled as a combination of 2nd degree polynomial functions and a fraction of a sphere, while their edges are rounded with a user-defined radius. In line with their inherent restriction to convexity, rather common in DEM with complex shapes, e.g. as in [8], the additional consideration of using potential particles will illustrate the mechanical implications of neglecting the concavity of the physical particles to the AOR.

For the exact definition of a potential particle, as detailed in Boon et al. [20], a set of N planes are assembled such that their normal vectors point outwards, with their interior forming a convex polytope. These planes are summed quadratically and expanded by a distance r, which is also related to the radius of the curvature at the corners.

Table 1: Default configuration of AOR simulations

Configuration	Initial number of particles	Side wall velocity	Container height	Container width
Axisymmetric	$N_{part} = 2,468$	$V_{cyl} = 6.67 \cdot 10^{-4}\ m/s$	$H_{cyl} = 9 \cdot 10^{-2}\ m$	$R_{cyl} = 8 \cdot 10^{-2}\ m$
Plane strain	$N_{part} = 2,150$	$V_{par} = 4.3 \cdot 10^{-2}\ m/s$	$H_{par} = 1.9 \cdot 10^{-1}\ m$	$L_{par} = 1 \cdot 10^{-1}\ m$

Furthermore, a 'shadow' spherical term is added, where R is its radius and $0 < k \leq 1$ denotes the fraction of sphericity of the particle. A value of $k \approx 0$ corresponds to a nearly sharp polyhedron, while $k = 1$ corresponds to a perfectly spherical particle.

A potential particle is eventually defined by a potential function f as in Equation 1:

$$f(x,y,z) = (1-k)\left(\sum_{i=1}^{N} \frac{\langle a_i x + b_i y + c_i z - d_i \rangle^2}{r^2} - 1\right) + k\left(\frac{x^2+y^2+z^2}{R^2} - 1\right) \tag{1}$$

where (a_i, b_i, c_i) is the normal vector of the i^{th} plane in local particle coordinates, d_i is the distance of the plane to the local origin and $\langle\ \rangle$ are Macaulay brackets, i.e., $\langle x \rangle = x$ for $x > 0$; $\langle x \rangle = 0$ for $x \leq 0$.

This potential function takes zero values ($f = 0$) on the particle surface, negative values ($f < 0$) inside the particle and positive values ($f > 0$) outside. In this sense, some similarity can be found with the Level-Set Discrete Element Method (LS-DEM) [21, 22, 23] where the potential is the actual distance function, unlike here. The contact point between two potential particles is found as the optimal point of a Second Order Conic optimisation Problem (SOCP) describing the contact detection problem, representing a point nearest to both the particles, based on their potential functions.

Here, the mathematical formulation of the potential particles enables one to approximate the given particle shape by a rounded tetrahedron. To decide which planes to use in order to assemble the potential particle of the 3D-printed material, two criteria were considered, a physical and a practical one, with the latter aiming to achieve post-processing convenience: (1) First, the potential particle should capture the morphology of the physical particle as faithfully as possible in terms of size, surface curvature, mass and inertia of the given physical particle, or other shape descriptors such as the sphericity; (2) To achieve comparable results with the clump models, for the evaluation of the AOR, it is convenient for each potential particle to be monitored via four points being located at the same positions than the centers of the four spheres making the tetrahedron. Thus, it is sought that the potential particle has a straightforward analogy to this format. To satisfy these criteria,

Table 2: Coefficients defining the planes making the faces of the tetrahedral potential particle as described in Equation 1.

Plane coefficient	Plane 1	Plane 2	Plane 3	Plane 4
a	0	$\sqrt{2/3}$	0	$-\sqrt{2/3}$
b	0	$\sqrt{2}/3$	$2\sqrt{2}/3$	$\sqrt{2}/3$
c	-1	1/3	1/3	1/3
d (cm)	0.063299	0.063299	0.063299	0.063299

the planes used to assemble the potential particle were chosen as the faces of the tetrahedron connecting the centers of the spheres making the physical particle (see Table 2). This approach can be generalised to approximate any convex shape, given a tessellation of its surface, or a multi-sphere representation of a particle made of spheres with equal radii.

To match the local surface curvature of the physical particle, a radius $r = r_s$ was chosen in Equation 1 to control the roundness of the edges and corners of the potential particle consistently with the r_s radius of each individual sphere in the physical particle. The radius of the shadow particle was assigned to $R = \sqrt{2}r_s$, to capture the curvature of faces of the given particle shape. The remaining parameter needed to be calibrated in order to match the given particle shape was the parameter k, which controls the curvature of the faces. A value of $k = 0.65$ led to a good match with the target geometry, i.e. it achieves an adequate representation of both the overall form of the real particle and features such as its main dimensions, while also approximating its curvature. The parameters r, R and k were chosen via a trial-and-error procedure. Figure 4 demonstrates visually the geometrical faithfulness of the generated potential particle to the shape of the real, physical particle.

In addition to modelling the rounded, tetrahedral-like particles, the potential particles also serve to simulate cuboidal elements of various sizes, making the moving and still parts of the plane-strain and axisymmetric devices, enabling one to build YADE models using a single, unified approach and contact detection algorithm.

2.2.3 Particle shape characterisation

As demonstrated in Figure 4, the selected potential particle can approximate the morphology of the physical particle faithfully, as it qualitatively represents the main dimensions of the particle, determining particle form, along with the curvatures of its edges/corners, relating to particle roundness. However, the potential particles modelling approach cannot represent the concavity of the physical particle. A quantitative characterisation of particle form was also performed using `SHAPE` [24], an open-source shape analysis software for three-dimensional particles, in order to quantify in Table 3 the similarity between the physical particle and its two numerical replicates. To this end, the surface mesh of the physical particle was first tessellated from its corresponding DEM

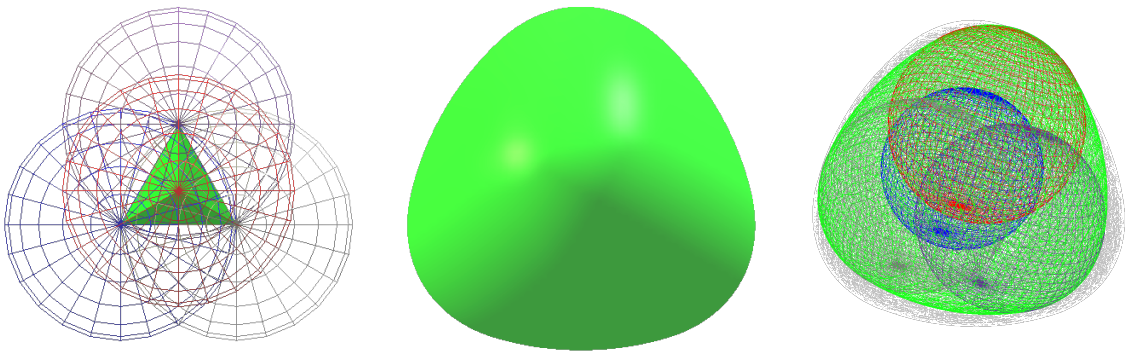

Fig. 4: Clumped tetrahedral particle (left); fitted potential particle (middle); overlap of the two (right).

clump, using the surface extraction module of `CLUMP` [17], an open-source code for the generation and processing of multi-sphere particles. Particle shape was characterised in terms of volume, surface area, principal inertia values, convexity and true sphericity. Convexity is calculated in [0;1] as the ratio of the volume of each particle divided by the volume of its convex hull, while true sphericity, also ranging in [0;1], is the ratio of the surface area of a sphere with equal volume to the surface area of the particle [25]. It becomes evident from Table 3 that both the physical and the potential particle take high values of convexity and true sphericity (>0.90). It may furthermore be noted that both the multi-sphere and the potential particle share the same minimal bounding box and thus main particle dimensions, resulting to the same flatness and elongation values considering indices that rely on these main particle dimensions. Therefore, flatness and elongation were not monitored in this study, as convexity and true sphericity were the two differentiating factors between the two studied particle representations, from a morphological standpoint. Table 3 also offers a comparison with a so-called "non-uniform density" clump approach that would count multiple times the overlapping parts of the sphere-members in the calculation of volume and inertia, which would correspond to density showing a spatial increase at areas where spheres overlap.

As expected, the considered potential particle has larger values of volume and geometric inertia. The effect of the resulting increased particle mass is investigated in Section 4.1 by scaling down their density so the potential particle has the same mass as the real particle, i.e. $\rho_{rescaled} = \rho \times 3.3304 \times 10^{-7}/(3.9248 \times 10^{-7}) \approx 943\ kg/m^3$.

Bringing the error on mass down to zero through this scaling, the error in inertia values for potential particles drops from 27.17 % down to 7.96 %. It is interesting to note that using overlapping spheres with no correction for uniform

Table 3: Shape parameters of the physical particle in comparison with various DEM approaches

Shape characteristics	(1) Physical particle or present clump approach	(2) Potential Particle	(2)-(1)/(1)	(3) Clump approach with non-uniform density	(3)-(1)/(1)
Volume (m^3)	3.3304×10^{-7}	$3.9248\ 10^{-7}$	17.85%	4.9965×10^{-7}	50.03%
Surface area (m^2)	2.491×10^{-4}	2.632×10^{-4}	5.66%	2.491×10^{-4}	0
Inertia tensor/ρ (m^5)	$\begin{bmatrix} 2.584 & 0 & 0 \\ 0 & 2.584 & 0 \\ 0 & 0 & 2.584 \end{bmatrix} \times 10^{-12}$	$\begin{bmatrix} 3.286 & 0 & 0 \\ 0 & 3.286 & 0 \\ 0 & 0 & 3.286 \end{bmatrix} \times 10^{-12}$	27.17%	$\begin{bmatrix} 3.123 & 0 & 0 \\ 0 & 3.123 & 0 \\ 0 & 0 & 3.123 \end{bmatrix} \times 10^{-12}$	20.86%
Convexity	0.954	1	4.82%	0.954	0
True sphericity	0.9328	0.9849	5.59%	0.9328	0

density i.e. inner overlaps would lead to an error of 50.03 % for the volume and 20.86 % for the eigenvalues of the principal inertia tensor.

2.3 DEM contact formulation

At each contact, kinematics is defined with the normal and tangential relative displacements of the particles, u_n and $\underline{u_t}$ respectively. For the clump model, contacts are detected between spheres belonging to different clumps and u_n is computed as the norm of the branch vector to the spheres' radii, while $\underline{u_t}$ is computed incrementally, see e.g. [23]. For the potential particle model, u_n is computed using a bracketed line-search algorithm as detailed in Boon et al. [20], deployed along the contact normal direction and starting from the contact point, to detect two points on the surface of each particle, forming a branch vector, the norm of which is considered as the sought approaching distance. The shear increment of $\underline{u_t}$ is calculated in a similar manner as for spheres, i.e. via time integration of the shear component of the relative velocity during contact.

The same contact model applies to these kinematic quantities for both the clump and the potential particle approaches, accounting for linear visco-elasticity and friction (Figure 5). In the normal direction, a spring with a normal stiffness K_n is associated in parallel with a viscous damper of coefficient c_n, as formulated in Equation 2. In the tangential direction, a spring with a tangential stiffness K_t is associated in series with a frictional slider (contact friction angle φ), see Equation 3.

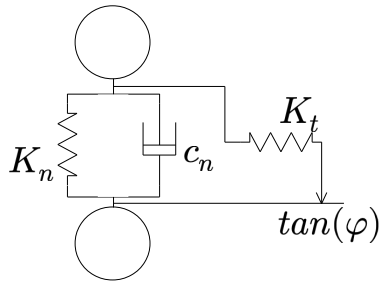

Fig. 5: Contact model with visco-elasticity and friction.

$$F_n = \max(K_n u_n + c_n \dot{u_n}, 0) \quad (2)$$

$$|\underline{F_t}| = \min(K_t |\underline{u_t}|, F_n \tan(\varphi)) \quad (3)$$

One should note that different YADE classes implement the above Eqs. 2-3 for clumps and potential particles with different methods of expressing the viscous damping coefficient c_n. In all cases, a desired normal restitution coefficient e_n serves a starting point before some differences appear in the YADE workflow, as detailed in Appendix A. Nevertheless, Figure 6 illustrates the common dissipative behavior of both models with the same $F_n(u_n)$ curves in the case of two colliding spheres (obtained after using $k = 1$ in Equation 1 for the PP approach) with an initial relative normal velocity V, demonstrating the consistency of the two implementations of visco-elasticity.

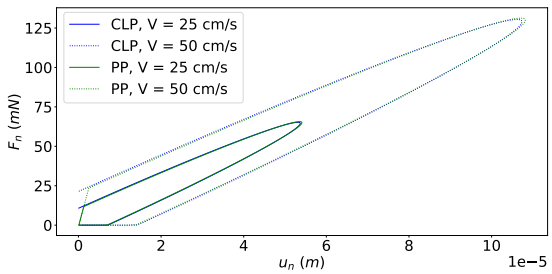

Fig. 6: Contact behaviour for different impact velocities in the two DEM approaches.

In the framework of the round robin test, the JGS measured the contact friction angle φ and the normal restitution coefficient e_n for resin against acrylic contacts and for resin against resin contacts, as well as the normal stiffness K_n for resin spheres. Experimental measurements exhibited a variability and are thus given as distributions (see Figure 7). Unless specified otherwise, the DEM clump simulations are defined accordingly, assigning to all contacts random values of φ and c_n which respect the same distributions.

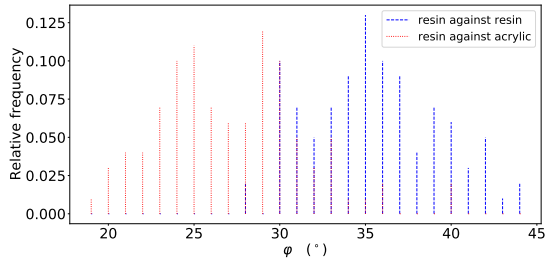

(a) Contact friction angles for particle/particle ($\varphi_{p/p}$) or particle/wall ($\varphi_{p/w}$) contacts

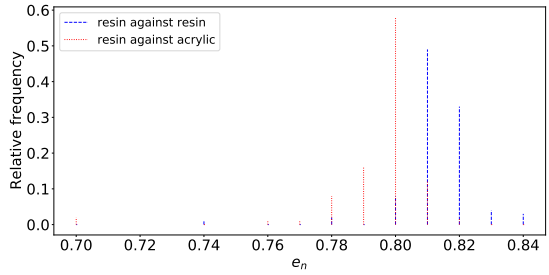

(b) Restitution coefficient

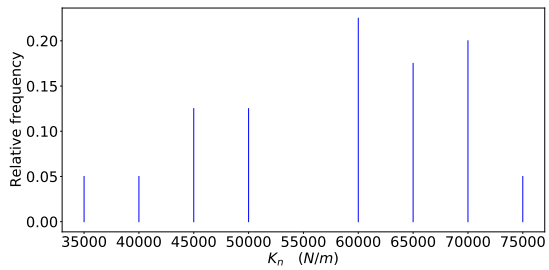

(c) Normal stiffness

Fig. 7: Distributions of contact properties as experimentally measured by the JGS (adapted from [4])

2.4 DEM simulation workflow

Building DEM samples starts with generating randomly in space particles inside the cuboidal or cylindrical containers mentioned in the above

Section 2.1, so as to form a extremely loose assembly of non-overlapping particles. The assembly is then deposited under its own weight until it becomes stable, and is saved to be subsequently used under different conditions. Different samples can be obtained starting from different initial particle arrangements. For this first step that has no experimental counterpart, an extra, non-physical, damping source is added in the local, non-viscous, form (Cundall's damping) to speed up the generation. For the rest of the simulations, contact-scale viscous damper and friction solely ensure the stabilisation of the simulations and no other source of damping is used.

The actual AOR simulation starts from this initial state by displacing the moving parts of the container in a manner equivalent to the experiments. Particles leaving the container from its periphery are counted as so-called lost particles and erased for computational efficiency. The simulation continues until the sample finds a new equilibrium in the form of a static heap. It is then possible to measure the angle between its exterior surface and the horizontal plane following the procedures discussed below.

The default set of parameters for this numerical setup is the experimental one previously given in Table 1.

3 Methodological discussion

3.1 Computational aspects of each modelling approach

In order to provide an overlook of the computational implications of the two considered DEM strategies for shape description, Figure 8 gives a comparison of the computation performances observed during 30 different simulations with both modelling approaches, in terms of computation speed S and Cundall's number $N_C = N_{part}S$. These simulations, presented in more details in Section 4.3, were run sequentially using a Intel(R) Xeon(R) Platinum 8270 CPU @ 2.70GHz with 1.5 TB of RAM available. Note that during all series of simulations in this paper the CPU cache wasn't controlled. Its capacity of 35.75 MB may thus not have been used as much over all simulations, making the time measurements somewhat biased.

Note that heaps may reach equilibrium at different simulated times; as a consequence, less and less values were available to compute the mean and standard deviation, until eventually there was only one. The results show that for these simulations, the clump model is approximately 100 times faster than the potential particle model. Considering that the present physical particles are simple to describe in a clump approach, using only 4

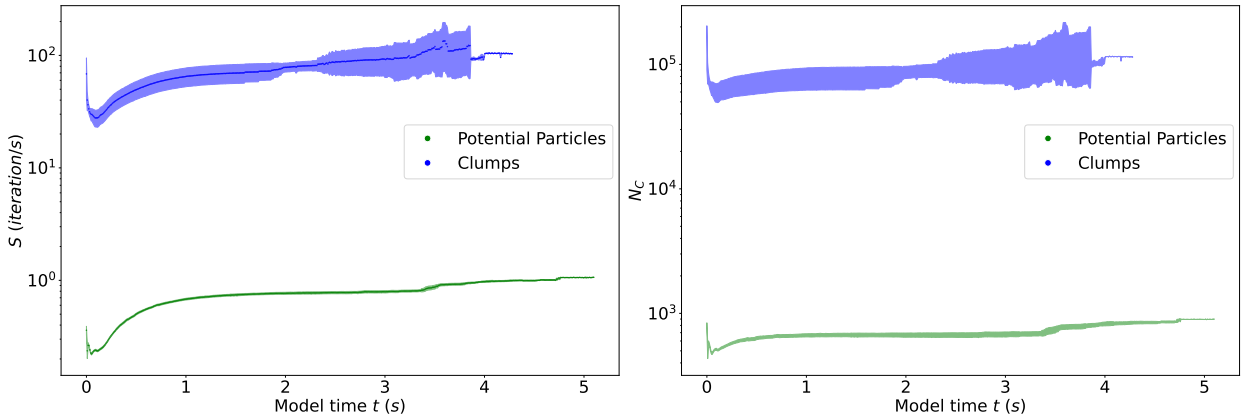

(a) Computation speed

(b) Cundall's number

Fig. 8: Computation speed statistics during 30 simulations with each DEM approach (either potential particles or clump, see Section 4.3 for details). Dots represent the mean speed value with the surrounding filled area corresponding to its standard deviation.

spherical members, the increased effort in computational time when using potential particles is in a classical order of magnitude for DEM approaches for non-spherical particles [23].

3.2 A systematic determination of the angle of repose

This section proposes two rigorous methods to measure the AOR, first, by defining an outer surface of particles and second, by computing an angle from these particles positions.

3.2.1 Outer surface detection

In the axisymmetric case (respectively plane strain case), the 3D space is discretized in several subdomains $\{r;\ \theta \in [\theta_a, \theta_b];\ z \in [z_a, z_b]\}$ (respectively $\{x \in [x_a, x_b];\ y \in [y_a, y_b], z\}$), giving an intersection with the outer surface at $max(r)$ (respectively $max(z)$) in each subdomain. The extent of each interval is selected such that only one particle should be therein detected as belonging to the outer surface. For such a purpose, length scales L_η are used for the coordinates θ, z in the axisymmetric case and x, y in the plane strain case. The index η can represent each of these coordinates. The number of intervals on each coordinate is then:

$$N_\eta = \frac{L_\eta}{d_{clump}} - 1 \tag{4}$$

with $L_\theta = 2\pi R_{cyl}$, $L_z = H_{cyl}$, $L_x = L_{par}$, and $L_y = H_{par}$.

$$\theta_a^i = i\frac{2\pi}{N_\theta};\quad \theta_b^i = (i+1)\frac{2\pi}{N_\theta} \tag{5}$$
$$\text{with}\quad i \in [\![0;\ N_\theta]\!]$$
$$\eta_a^i = i\frac{L_\eta}{N_\eta};\quad \eta_b^i = (i+1)\frac{L_\eta}{N_\eta} \tag{6}$$
$$\text{with}\quad i \in [\![0;\ N_\eta]\!], \eta \in \{x, y, z\}$$

Figure 9 shows a typical result after detecting all the particles belonging to the outer surface in both configurations. Note that gravity has the opposite orientation of the z-axis.

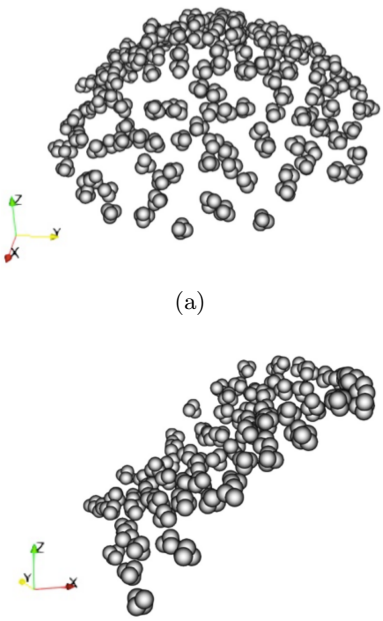

(a)

(b)

Fig. 9: Outer surface in the axisymmetric (a) and plane strain configurations (b).

3.2.2 Angle of repose measurement

From this point the method is the same in both heap configurations except for the orientation of the horizontal axis. The coordinates $(\widetilde{x},\ \widetilde{y},\ \widetilde{z})$ will thus denote respectively $(-r,\ z,\ \theta)$ in the axisymmetric case or $(x,\ z,\ y)$ in the plane strain case. The width of the container $\widetilde{x}_{box}$ for instance stands for R_{cyl} in the axisymmetric case and L_{par} in the plane strain case.

Assuming a $\widetilde{z}$-invariance of the heaps, we project the spheres on the $(\widetilde{x},\ \widetilde{y})$ planes (see Figure 10) and perform a linear regression on the resulting points to determine the AOR α. Letting the linear regression be $\widetilde{y}_1 = a_1\widetilde{x} + b_1$, one has:

$$\alpha = \arctan(a_1) \tag{7}$$

Consistently with [13, 14], one can notice that the surface isn't exactly flat but slightly curved (especially in the axisymmetric configuration). It can thus be useful to compute a second degree regression as well in order to fit the outer surface in the best possible way. Letting the second degree regression be $\widetilde{y}_2 = a_2\widetilde{x}^2 + b_2\widetilde{x} + c_2$, one can compute a local angle:

$$\alpha(\widetilde{x}) = \arctan(2a_2\widetilde{x} + b_2) \tag{8}$$

To make the measurement more meaningful, one may naturally restrict the procedure to a smaller zone of the heap: the particles considered in the regressions would only be the ones inside an interval $[\widetilde{x}_{min}, \widetilde{x}_{max}]$. Indeed, the lower particles may be abruptly blocked by the bottom ridge of the container devices and should be excluded from the measurement. Also, particles with a high $\widetilde{x}$, away from the opened boundary, could be unaffected by the discharge and still form a horizontal

surface, especially in the axisymmetric configuration. Indeed, finite particle-size effects necessarily exist and affect the transition from one side of the slope to another.

Excluding from the bottom of the heap the few particles that are stuck by the ridge, and only those, is obtained choosing: $\widetilde{x}_{min} = 0.32 d_{clump}$. An appropriate value for $\widetilde{x}_{max}$ is sought by measuring α for several $\widetilde{x}_{max}$. The best $\widetilde{x}_{max}$ is the smallest for which the measurement does not change. The error on the measurement is also a criterion to choose the best $\widetilde{x}_{max}$. This method should be specially relevant in the axisymmetric case since the outer surface is curved, but it should work on the plane strain heap as well.

3.2.3 Error on the measurement

For a given heap, the dispersion of positions data induces some error on the linear regression and the measurement of α. As an alternative to the correlation coefficient R^2, this error can be quantified from a standard deviation on the slope a_1 of the fitting line, $\mathrm{StD}(a_1)$. If N is the number of points and $(\widetilde{x}_i,\ \widetilde{y}_i)$ are the coordinates of the i^{th} point, one has:

$$\mathrm{StD}(a_1) = \sqrt{\frac{1}{N-2}\frac{\sum_{i=1}^{N}(a_1\widetilde{x}_i + b_1 - \widetilde{y}_i)^2}{\sum_{i=1}^{N}(\widetilde{x}_i - \overline{\widetilde{x}})^2}} \quad (9)$$

(10)

which, considering Equation 7, gives the standard deviation on the angle, $\mathrm{StD}(\alpha)$:

$$\mathrm{StD}(\alpha) = \frac{\mathrm{StD}(a_1)}{1 + {a_1}^2} \quad (11)$$

Figure 10 shows the regressions made on the projection of the outer surface in both configurations and the resulting angle for $\widetilde{x}_{max}/\widetilde{x}_{box} = 0.4$, with $\widetilde{x}_{box} \in \{R_{cyl}, L_{par}\}$. Figure 11 shows measurements performed for several $\widetilde{x}_{max}$ in both configurations. The error bars represent the error computed with Equation 11. One can see that the AOR increases with $\widetilde{x}_{max}$, except for very high values of $\widetilde{x}_{max}$ where the part of the outer surface considered is very small compared to its size. This may be caused by the ridge on the bottom of the open container that maintains some particles, affecting the geometry of the outer surface. The error on the measurement is very low but increases with $\widetilde{x}_{max}$. The measurement is more stable for low $\widetilde{x}_{max}$, specially in the axisymmetric case. From now on, the measurements will be performed on most of the outer surface, using $\widetilde{x}_{min} = 0.32 d_{clump}$ and $\widetilde{x}_{max} = \widetilde{x}_{box}$.

3.2.4 Error due to repeatability

The simulations performed with the clump model include two sources of randomness. The first one is the initial configuration of the sample, with random positions for the particles in the initial cloud.

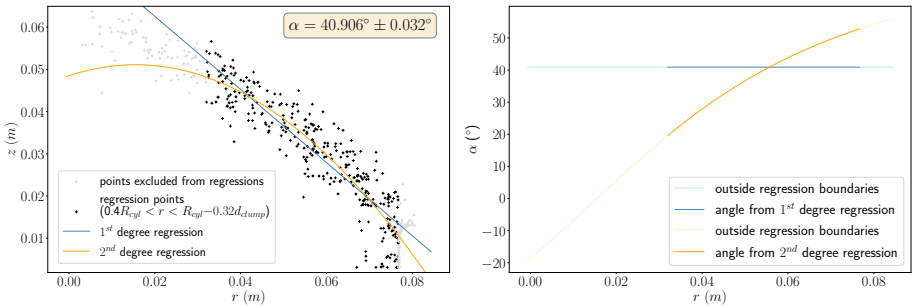

(a) Projection of the outer surface (axisymmetric configuration)

(b) Local angle (axisymmetric configuration)

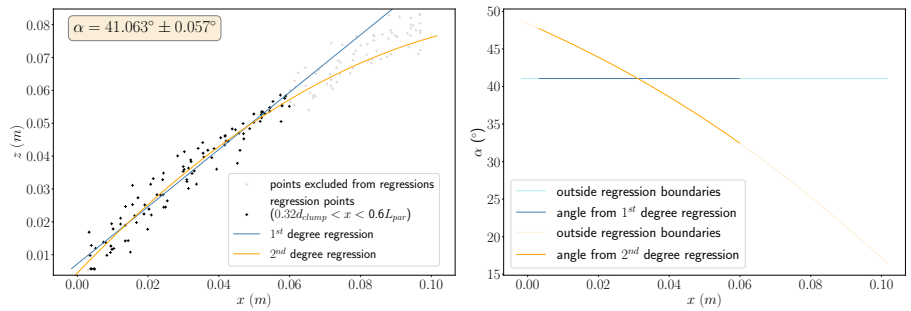

(c) Projection of the outer surface (plane strain configuration)

(d) Local angle (plane strain configuration)

Fig. 10: Outer surface regressions for an intermediate $\widetilde{x}_{min}$ and the associated measurement ((a), (c)) in both configurations.

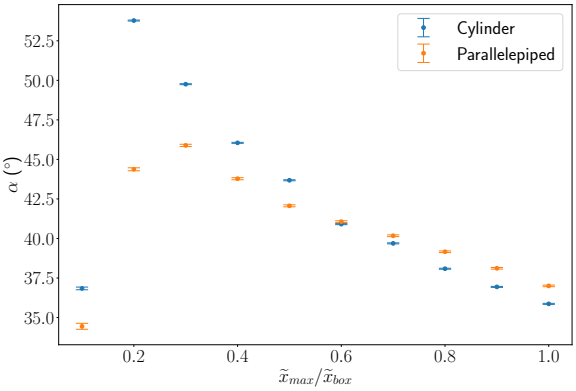

Fig. 11: Average slope as measured for different values of $\widetilde{x}_{max}$.

The second source lies in the statistical distribution of contact properties (see the above Figure 7). Indeed, the use of distributions for φ and e_n implies choosing a different value for each contact, all values being randomly chosen according to the given probability distribution. If one was to swap the values of two contacts, the distribution would still be respected, but the conditions of the simulation would be different, introducing randomness.

In order to quantify the repeatability error, a series of simulations was performed with the clump model using 30 different values for the seed parameter, the particles in the initial samples of each simulation thus have different positions and contact properties. This series will be called

CLP1 and uses the default parameters of Table 4. Among those parameters, the time step is computed from contact stiffnesses and particle masses following [26]. Note that all samples have approximately the same initial densities. Figure 12 shows the AOR measured using CLP1 heaps and one can see that the variation in the measurement is lower than 3%. Even though such a repeatability error is low, it will be systematically given for all series of simulations in this paper as error bars on the AOR charts.

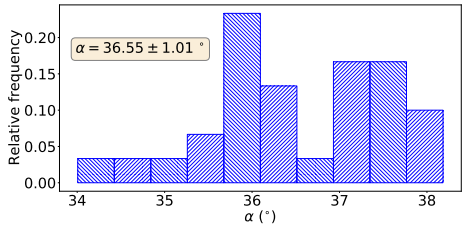

(a) Plane strain

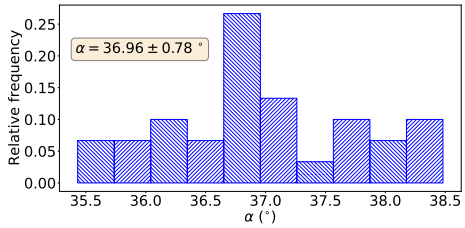

(b) Axisymmetric

Fig. 12: Distributions of measured angles of repose when investigating repeatability in the CLP1 configurations of Table 4.

3.3 Measuring the void ratio for any geometry of assembly

With respect to the objective of discussing the possible constitutive nature of the AOR determined as per Section 3.2, it is interesting to characterize the state of the heap in terms of density or void ratio e, as a fundamental parameter of granular materials. This density characterization is not straightforward because of the irregular geometry of the heap along its free surface, and possible bias caused by an excess of void near the walls

As such, two methods are proposed below to compute the void ratio inside a granular assembly with a complex geometry, while avoiding the boundary effects: a so-called "tetrahedra method" and a "sub-volume method". Both methods provide local values for e and rely on a Monte Carlo procedure to compute volume proportions, combined with (straightforward, here) tests to determine whether a random point in space is inside a physical particle. The following differences still exist, though:

- the tetrahedra method applies for any geometry of sample with no requirements on the geometry. It is based on a triangulation of the sample.
- the sub-volume method requires to define an homothetic sub-volume inside the sample,

Table 4: Parameters for heap simulations investigating repeatability (CLP1 series, 60 simulations in total).

Configuration	N_{part}	K_n $(N.m^{-1})$	K_s/K_n	ρ $(kg.m^{-3})$	Δt (s)	φ	e_0	Number of samples
Plane strain	$2,150$	$58,250$	0.37	$1,111$	7.86×10^{-5}	see Figure 7	0.622 ± 0.012	30
Axisymmetric	$2,468$						0.744 ± 0.028	

which can be difficult if the latter adopts a peculiar geometry. However, it is substantially faster than the tetrahedra method.

3.3.1 The tetrahedra method

In order to compute a void ratio on a heap with a random geometry, the tetrahedra method starts by a triangulation of the heap. The Monte Carlo method is then used to determine the proportion of particles inside each tetrahedron resulting from the triangulation, leading to an expression for the void ratio.

3.3.1.1 Triangulating the heap

This first step is done using Delaunay's triangulation on the centers of all particles, although it could be done using another set of relevant points (e.g. the center of all spheres for clump simulations). Also, one should keep in mind that when triangulating using the center of the particles a small part of the sample is ignored: all particles on the outer surfaces are cut by the boundary tetrahedra. This should effectively remove the excess of void near the walls of any sample. The set of all tetrahedra will be denoted $\{tet\}$.

3.3.1.2 Detecting which particle may be partially inside each tetrahedron

All particles bounding boxes are tested to determine if they overlap a tetrahedron bounding box. If so, the particle is further checked for intersected volume with the Monte Carlo method, forming a set of particles that is denoted $\{p\}^{cut}$. This step is not mandatory but it drastically reduces the computation time.

3.3.1.3 Computing the total volume of particle inside each tetrahedron

In this final step, N_{mc} points $\{\underline{x_i}, i \in [1, N_{mc}] \cap \mathbb{N}\}$ are uniformly drawn inside the tetrahedron, following [27]. Each point is tested to determine if it is located inside any of the particles potentially cut $\{p\}^{cut}$. Denoting V^{tet} the volume of a tetrahedron tet computed using its vertices' coordinates; $\chi^p(\underline{x})$ the Boolean test function equal to

1 if the point $\underline{x}$ is inside the particle p, 0 otherwise; and $H(n)$ the Heaviside function, the Monte-Carlo method gives the total volume of particle inside the tetrahedron as follows:

$$V_{part}^{tet} = \frac{\sum_{i=1}^{N_{mc}} H\left(\sum_{\{p\}^{cut}} \chi^p(\underline{x}_i)\right)}{N_{mc}} \times V^{tet} \quad (12)$$

A local void ratio can then be computed for the tetrahedron:

$$e^{tet} = \frac{V^{tet} - V_{part}^{tet}}{V_{part}^{tet}} \quad (13)$$

And globally:

$$V_{part} = \sum_{\{tet\}} V_{part}^{tet} \quad (14)$$

$$V_{tot} = \sum_{\{tet\}} V^{tet} \quad (15)$$

$$e = \frac{V_{tot} - V_{part}}{V_{part}} \quad (16)$$

Taking advantage of the independence between operations in each tetrahedron, the proposed implementation of this method is parallel with an almost optimal speed-up: the increase in execution speed is close to the number of processes running at the same time.

3.3.2 The sub-volume method

The sub-volume method consists in three steps detailed below.

3.3.2.1 Defining the sub-volume

This step is illustrated using the two samples' geometries considered in this paper. The sub-volume is chosen as a homothetic transformation of the heap centered in the sample, for both configurations. The sub-volume and the total volume of the sample will be denoted V_{sub} and V, respectively. At the final state, the geometry of the sample is assumed to be a half parallelepiped (respectively a cone) for the plane strain (respectively axisymmetric) configuration. The sub-volume is defined using a parameter C that pilots the homothetic transformation. The coordinates of the sub-volume axis aligned bounding box are denoted $\left(x_{min},\, y_{min},\, z_{min}\right)$ and $\left(x_{max},\, y_{max},\, z_{max}\right)$ and depend on the coordinates of the sample axis aligned bounding box: $\left(X_{min},\, Y_{min},\, Z_{min}\right)$ and $\left(X_{max},\, Y_{max},\, Z_{max}\right)$.

In the case of the plane strain configuration, the homothetic sub-volume can be determined as follows (Figure 13):

$$s_{min} = (1 - C)(S_{max} - S_{min}) + S_{min} \quad (17)$$

$$s_{max} = C(S_{max} - S_{min}) + S_{min} \quad (18)$$

with $\forall (s, S) \in \{(x, X), (y, Y), (z, Z)\}$ and $\forall C \in]0.5, 1]$.

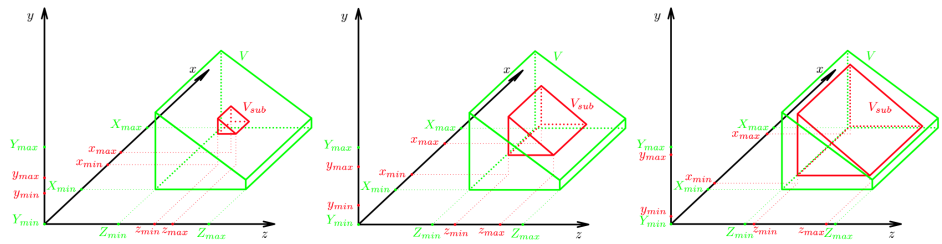

(a) $C = 0.6$ (b) $C = 0.75$ (c) $C = 0.9$

Fig. 13: Illustration of sub-volume for several C values in the plane strain configuration.

In the case of the axisymmetric configuration, one has to compute the x and y coordinates of the center, x_Ω and y_Ω respectively, and the maximum radius r_c of the cone (Figure 14). The homothetic sub-volume is then:

$$z_{min} = (1 - C)(Z_{max} - Z_{min}) + Z_{min} \tag{19}$$

$$z_{max} = C(Z_{max} - Z_{min}) + Z_{min} \tag{20}$$

$$s_\Omega = \frac{S_{min} + S_{max}}{2} \tag{21}$$

$$r_c = (2C - 1)\frac{X_{max} - X_{min} + Y_{max} - Y_{min}}{4} \tag{22}$$

with $\forall (s, S) \in \{(x, X), (y, Y)\}$ and $\forall C \in]0.5, 1]$.

3.3.2.2 Counting the volume of particles completely inside the sub-volume

During this step, the 8 vertices $\underline{x}_i^p$ of a particle axis aligned bounding box are tested to determine if they are part of the sub-volume. Using the $\chi^{sub}(\underline{x})$ function, the number of vertices inside the sub-volume for a particle p reads:

$$N_{in}^p = \sum_{i=1}^{8} \chi^{sub}(\underline{x}_i^p) \tag{23}$$

If $N_{in}^p = 8$, the particle p is completely inside the sub-volume while if $N_{in}^p = 0$ the particle p is completely outside the sub-volume.

Denoting V^p the volume of the particle p, the total volume of particles completely inside the sub-volume is:

$$V_{part}^{in} = \sum_{\{p \ | \ N_{in}^p = 8\}} V^p \tag{24}$$

3.3.2.3 Counting the volume of particles partially inside the sub-volume

If $0 < N_{in}^p < 8$, the particle may be cut by the faces of the sub-volume. The proportion of the particle volume inside the sub-volume is again determined using the Monte Carlo method: N_{mc} points, $\{\underline{x}_i, i \in [\![1;\ N_{mc}]\!]\}$, are uniformly drawn inside the particle bounding box and tested to

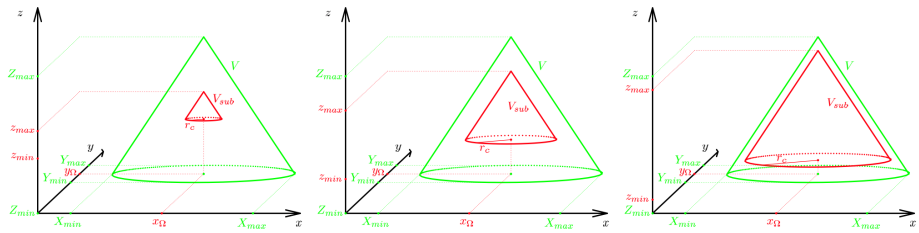

(a) $C = 0.6$ (b) $C = 0.75$ (c) $C = 0.9$

Fig. 14: Illustration of sub-volume for several C values in the axisymmetric case.

determine if they are simultaneously inside the sub-volume (test function $\chi^{sub}(\underline{x}_i)$) and inside the particle (test function $\chi^{p}(\underline{x}_i)$). The proportion of a particle volume being also part of the sub-volume is then:

$$V_{in}^{p} = \frac{\sum_{i=1}^{N_{mc}} \chi^{sub}(\underline{x}_i)\chi^{p}(\underline{x}_i)}{N_{mc}} \times V^{p} \tag{25}$$

The total volume of particles partially inside the sub-volume is:

$$V_{part}^{cut} = \sum_{\{p \ | \ 0<N_{in}^{p}<8\}} V_{in}^{p} \tag{26}$$

The total volume of particle inside the sub-volume then reads:

$$V_{part} = V_{part}^{in} + V_{part}^{cut} \tag{27}$$

Finally, the void ratio is determined by:

$$e = \frac{V_{sub} - V_{part}}{V_{part}} \tag{28}$$

For the simplest sub-volume geometries the expression of V_{sub} is trivial. In more complex situations it can be determined using once again the Monte Carlo method inside the sub-volume bounding box:

$$V_{sub}^{bb} = (x_{max} - x_{min})(y_{max} - y_{min})(z_{max} - z_{min}) \tag{29}$$

$$V_{sub} = \frac{\sum_{i=1}^{N_{mc}} \chi^{sub}(\underline{x}_i)}{N_{mc}} \times V_{sub}^{bb} \tag{30}$$

Both methods can be optimized when used with simple shapes (e.g. spheres): one could detect more precisely which particle may be cut. Also, one may be able to draw uniformly points directly inside the particle instead of the bounding box, making it possible to set aside the function χ^{p} and giving a more accurate Monte Carlo method.

3.3.3 Examples of void ratio measurements

3.3.3.1 Local void ratio

The tetrahedra method makes it possible to establish directly a local representation of the void ratio, as illustrated in Figure 15 for one plane strain final heap. One can notice that the geometry of the final heap is accurately captured by the triangulation, giving a rounded half parallelepipedic boundary surface. The density range is quite wide: some tetrahedra located on the outer surface, where the particles moved, contain approximately 1000 times more voids than other tetrahedra located where the particles almost didn't move. Note that this figure represents the void ratio directly interpolated from the centroids of each tetrahedron and thus should be interpreted carefully.

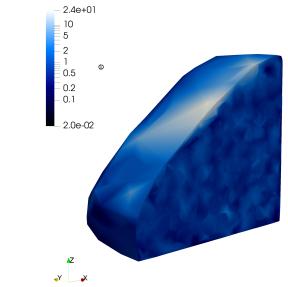

(a) Sliced view

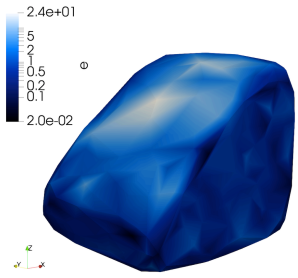

(b) Complete view

Fig. 15: Local void ratio in a plane strain final heap as measured with the tetrahedra method.

3.3.3.2 Parallel implementation of the tetrahedra method

The independence of the processing of each tetrahedron makes it possible to parallelize this method. A series of measurements was performed on 30 clump samples at their initial states (showing different individual locations of particles) using different numbers of CPU cores, $N_{cores} \geq 1$, on the same machine previously used in Section 3.1. The speed-up S and its standard deviation ΔS was computed from the computation times $T_{N_{cores}} \pm \Delta T_{N_{cores}}$ as follows:

$$S = \frac{T_1}{T_{N_{cores}}} \tag{31}$$

$$\Delta S = S\left(\frac{\Delta T_1}{T_1} + \frac{\Delta T_{N_{cores}}}{T_{N_{cores}}}\right) \tag{32}$$

Since the CPU cache was not precisely controlled, the total CPU load had an influence on the computation speed, which might lead to a speed-up seemingly above perfection in the eventuality of

the CPU cache being full during the measurement on 1 core and not for more cores.

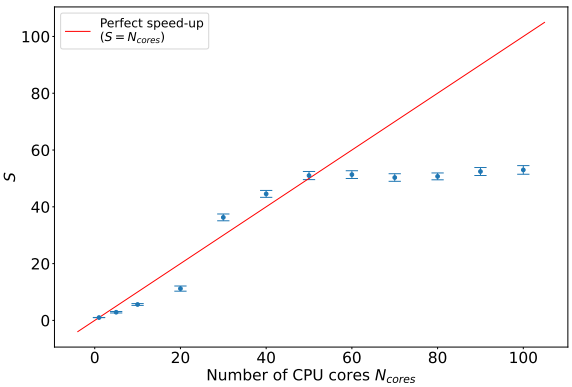

Fig. 16: Parallelization speed-up for the tetrahedra method.

Figure 16 shows the speed-up for $N_{cores} \in \{1, 5, 10, 20, 30, 40, 50, 60, 70, 80, 90, 100\}$. The speed-up stops to improve starting from $N_{cores} = 50$, which is probably due to an over usage of the CPU. A better control of the CPU could give more accurate speed-up measurements. Nevertheless, for $N_{cores} < 50$ the parallelization is optimum: $S \approx N_{cores}$.

3.3.3.3 Sub-volume and tetrahedra methods comparison

Void ratio measurements were performed for the clump model on all 30 initial samples of CLP1 plane-strain series of simulations, discussed in more details in Section 4.3. Because of the simple parallelepipedic geometry of these granular assemblies, a reference void ratio can be easily computed using the sample bounding box:

$$V_{tot} = (X_{max} - X_{min})(Y_{max} - Y_{min})(Z_{max} - Z_{min}) \quad (33)$$

$$V_{part} = \sum_{\{p\}} V^p \quad \text{, with } \{p\} \text{ the set of all particles} \quad (34)$$

$$e^{REF} = \frac{V_{tot} - V_{part}}{V_{part}} \quad (35)$$

Figure 17 (a) illustrates the comparison between the mean values and standard deviation over the 30 samples of e^{REF} together with e^{TET} for the tetrahedra method and e^{SUB} for the sub-volume method. The latter has been computed for 3 values of N_{mc} and 40 values of C.

For the lowest values of C, the measured e^{SUB} void ratio varies a lot among the 30 simulations and in function of N_{mc}. Between $C \approx 0.7$ and $C \approx 0.9$, e^{SUB} is constant and its standard deviation gets lower, being furthermore little dependent on N_{mc}. For $C > 0.9$, its mean value and standard deviation finally start to increase as expected due to the rigid boundaries constraining the granular assembly and favoring voids to form near the outer surfaces. Finally, for $C = 1$, the sub-volume method gives by definition the exact same values for void ratio than when using the global bounding box: $e^{SUB} = e^{REF}$.

The tetrahedra method gives a e^{TET} measurement being close to e^{SUB} when $0.7 < C < 0.9$, which suggests that it successfully excludes the excess of void from the computation.

As for the computational costs, Figure 17 (b) shows the corresponding execution times, t^{SUB}, t^{TET} and t^{REF}, while e^{TET} was computed using parallelization on 3 cores. One observes that, in spite of parallelization, the tetrahedra method is here significantly slower than the sub-volume method. Regarding the sub-volume method, using $N_{mc} = 1000$ instead of $N_{mc} = 100$ slows down considerably the computation for no gain in accuracy, especially for high values of C.

In view of these results, subsequent measurements of void ratio will be obtained using the sub-volume method with $N_{mc} = 100$ and $C = 0.8$.

4 Physical discussion

This section analyses the dependence of AOR on several parameters: the particle shape, the initial void ratio and the sample size. Experimental results obtained in [4] are also provided.

4.1 Parametric study

4.1.1 (Non-)Sensitivity to the tangential stiffness

A first series of simulations investigates the role of tangential stiffness when using the potential particles model and two different values of K_s: 240 N/m and 444 N/m (see sets B and C of Table 5).

Results are given in Figure 18 for what concerns the initial and final states of the samples. Most importantly, the two different values of tangential stiffness are shown to result in virtually the same AOR distribution. The $K_s = 240N.m^{-1}$ value will thus be kept in the remainder of the sequel for it results in a higher critical time step. One may furthermore note that the initial coordination number is slightly lower with a higher K_s, which is expected since stiff particles tend to be further away from each other, even when constrained. However, at the final state, the average coordination number is unaffected by K_s, certainly because they are not constrained enough for their relative distance to depend on K_s.

4.1.2 (Non-)Sensitivity to the particle mass density

While the AOR α refers to a static condition, the mass density of particles ρ physically affects the prior dynamic evolutions of the system. On the other hand, from a computational standpoint, the density also controls the critical time step of the

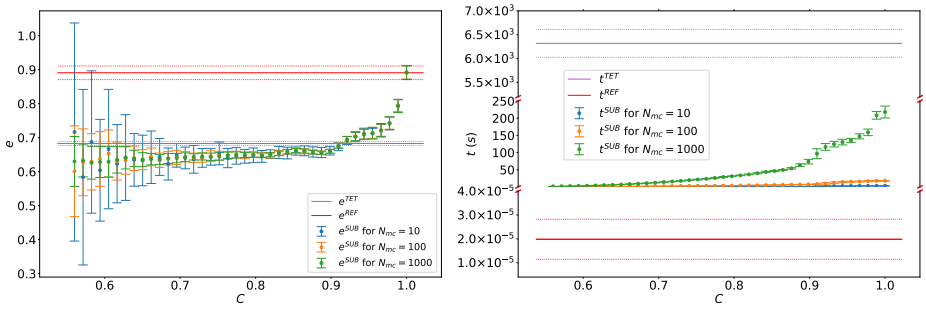

(a) Void ratio (b) Time cost

Fig. 17: Void ratio measurements with both methods for 30 parallelepipedic initial samples differing in individual locations of particles. On figure (b), the y axis is broken at two places: first between 40 ns and 50 ms, and second between 250 s and 5200 s. The three parts of the y axis do not have the same scale.

Table 5: Used parameters for the parametric study with potential particles - series PP1.

Set id	Configuration	K_n $(N.m^{-1})$	K_s/K_n	ρ $(kg.m^{-3})$	Δt (s)	$\varphi_{p/p}(^\circ)$	$\varphi_{p/w}(^\circ)$	β_n	Number of samples
A			0.2	1111	8.52×10^{-5}				
B	Plane strain	1,200	0.2	943	7.86×10^{-5}	35.5	27.2	0.071	30
C			0.37	943	7.86×10^{-5}				

present explicit DEM scheme and the total time cost. Other series of simulations with different ρ are thus proposed to check whether a variation from the experimental reference $\rho = 1,111\ kg/m^3$ would affect the AOR results.

Using potential particles, two values for the particle density are considered in the framework of the PP1 series (sets A and B of Table 5): the experimental one, $\rho = 1,111\ kg/m^3$, and $\rho = 943\ kg/m^3$ that would confer the potential particle the same mass as the physical particle in spite of the volume differences discussed in the above Section 2.2.3. Using clumps in a CLP2 series, four to seven different values for $\rho \in [100\ kg/m^3;\ 10,000\ kg/m^3]$ are considered, with 10 different initial samples in each case. Corresponding parameters are all given in Table 6.

Figure 19 shows the resulting angles of repose in the CLP2 and PP1 series, together with time costs of CLP1 series measured for a sequential execution on the same machine presented in previous Section 3.1. The dots correspond to the mean measurement over all samples for a given particle density and the error bars represent the standard deviation. One can see that all error bars share a common zone for a given shape description. As such, it is herein concluded, consistent to [9], that particle density does not impact the AOR. During DEM simulations, one can thus adopt, when necessary, an artificial $\rho = 10,000\ kg/m^3$, multiplying the critical time step by a factor of $\sqrt{\frac{10000}{1111}} \approx 3$

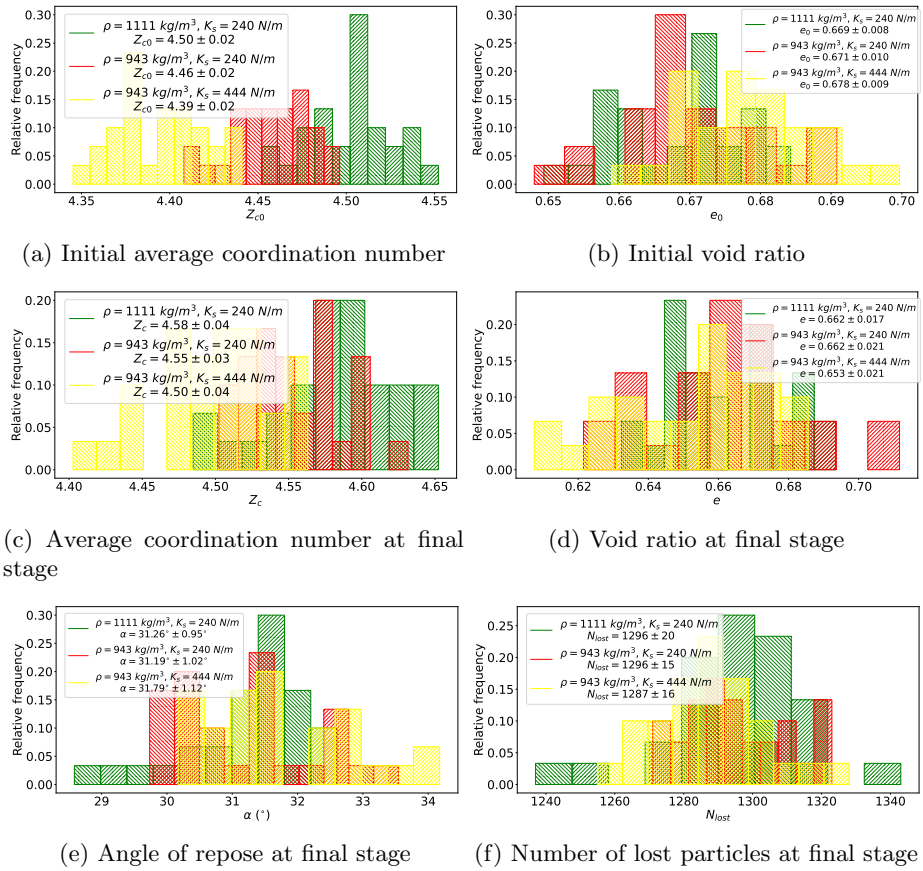

(a) Initial average coordination number

(b) Initial void ratio

(c) Average coordination number at final stage

(d) Void ratio at final stage

(e) Angle of repose at final stage

(f) Number of lost particles at final stage

Fig. 18: Macro-scale and micro-scale results of the parametric analysis with potential particles (PP1 series, Table 5).

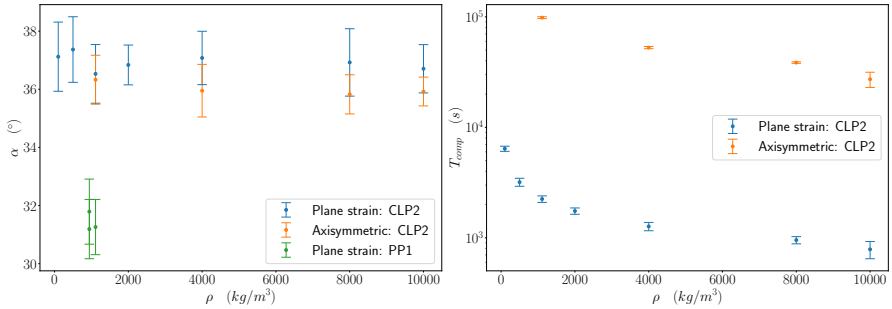

(a) Angle of repose

(b) Time cost

Fig. 19: Particle density influence on the angle of repose and on the time cost - CLP2 and PP1 series

and reducing as much the total time cost of the simulation (Figure 19b) until the heap stabilizes. In the Figure 19b, one can finally note a longer computation time for the axisymmetric configuration because of a lower velocity of the descending wall in the reference experiments.

Table 6: Parameters of heap simulations investigating ρ influence (CLP2 series, 110 simulations in total).

Configuration	N_{part}	ρ	e_0	Number of samples
Plane-strain	2,150	$100\ kg/m^3$	0.652 ± 0.011	10
		$500\ kg/m^3$	0.633 ± 0.010	
		$1,111\ kg/m^3$	0.623 ± 0.009	
		$2,000\ kg/m^3$	0.618 ± 0.010	
		$4,000\ kg/m^3$	0.607 ± 0.011	
		$8,000\ kg/m^3$	0.603 ± 0.012	
		$10,000\ kg/m^3$	0.603 ± 0.010	
Axisymmetric	2,468	$1,111\ kg/m^3$	0.743 ± 0.022	
		$4,000\ kg/m^3$	0.723 ± 0.015	
		$8,000\ kg/m^3$	0.709 ± 0.019	
		$10,000\ kg/m^3$	0.694 ± 0.010	

4.2 Numerical angle of repose vs experimental one

The numerical simulations are now compared with the experimental results provided at the end of the JGS round-robin and in [4]. In this framework, a simpler method was adopted to compute the AOR, considering only the highest particle instead of the whole external surface as in previous Section 3.2, for sake of simplicity during the experiments. In the axisymmetric configuration, slopes are actually determined in 360 directions being not exactly radial and their average is used to compute the AOR, while in the plane strain configuration the AOR is computed using only one slope direction in the plane.

In this subsection, the exact same method is adopted to interpret our numerical results for a consistent comparison. The set of parameters used for the clump model is the same as for CLP1 (see Table 4), and the set of parameters used for the potential particle model is given in Table 7.

Table 8 compares the obtained experimental and numerical results. In the plane strain configuration, the experimental AOR is approximately 8% higher than the one obtained for the clump model and 16% higher than the one obtained for the potential particle model. In the axisymmetric configuration, the experimental AOR is approximately 4% higher than the one obtained with the clump model and 16% higher than the one obtained for the potential particle model. Also, one should notice that in the plane strain configuration the JGS method measures an AOR higher than the method presented in this paper, and lower in the axisymmetric configuration (see Figure 12). This changes the conclusion on the influence of the configuration: with our measurement method both configurations gives the same AOR (difference of approximately 1% with the clump model), while the JGS method gives a difference of approximately 11%.

Table 7: Material properties used in the potential particles models.

K_n $(N.m^{-1})$	K_s/K_n	ρ $(kg.m^{-3})$	Δt (s)	$\varphi_{p/p}$ (°)	$\varphi_{p/w}$ (°)	β_n
1200	0.773	943	7.86×10^{-5}	35.5	27.2	0.071

Table 8: Angle of repose as per the JGS measurement method.

	Number of samples	Average (°)	Standard Deviation (°)	Minimum (°)	Maximum (°)
Plane strain configuration					
Experiments [4]	400	41.4	1.28	38.3	46.3
Clumps	100	38.1	1.14	35.0	41.3
Potential particles	18	34.8	1.61	32.5	38.0
Axisymmetric configuration					
Experiments [4]	50	35.3	0.9	33.3	37.3
Clumps	100	33.9	0.8	32.0	36.1
Potential particles	19	29.7	0.78	28.5	31.2

4.3 Role of particle concavity

The differences in AOR observed in Table 8 between the clump and potential particle (PP) models, with a higher discrepancy for PP towards experiments, certainly arise from the convex simplification of potential particles, with respect to the concavities of the physical particles which allow them to interlock better. In order to gain more insights into the influence of particle concavity, a rigorous comparison between the two numerical models is led in this subsection, adopting the same parameters for both models (except for the time step for computational efficiency) and determining the AOR using the more reliable method presented in Section 3.2. This series is called PP-CLP, with all parameters being listed in Table 9 and Table 10.

Figure 20 characterizes the initial and final states of these PP-CLP simulations. First and foremost, it is to notice that the AOR is approximately 14% lower with the potential particle model. This difference can be considered as significant and is even greater with respect to experiments even though the physical particles show a fairly high convexity of 0.954. In line with additional possibilities of interlocking for non-convex particles, while convex particles fall more easily from the heap, the number of lost particles is approximately 23% lower with the clump model. One can also note that the final void ratio is approximately the same with both models and

Table 9: Contact parameters of the PP-CLP series focusing on particle concavity

Model	K_n	K_s	e_n	$\varphi_{p/p}$	$\varphi_{p/w}$
Clump Potential particle	1.2 $kN.m^{-1}$	0.24 $kN.m^{-1}$	0.8	35.5°	27.2°

Table 10: Other simulation parameters of the PP-CLP series on particle concavity

Model	Configuration	ρ	Δt	Number of samples
Clump Potential particle	Plane strain	1111 $kg.m^{-3}$	$\approx 78.5\ \mu s$ $\approx 85.2\ \mu s$	30

that the final average number of contact points per particleis approximately 25% lower with the potential particle model since two convex particles can form only one contact point, unlike the concave clump.

It is worth noticing that the experimental measurement method gives a gap between the axisymmetric and plane strain configurations' angle of repose. The curvature of the axisymmetric heap explains the lower measurement obtained with the JGS method.

Looking at initial stages, one observes that the initial void ratio is approximately 5% lower with the clump model. The difference between the void ratio at the initial state and final state is interesting: at the initial state the sample is constrained by four side walls and one bottom wall, while at the final state one of the four side of the sample is free. This suggests that concave particles are more likely to fill the voids when there are surrounded by walls (parallel to the gravity axis), but when they are free to move, they do not fill the voids better than convex particles. On the other hand, the difference on the average number of contact points is approximately the same at the initial and final states.

4.4 (Non-)Constitutive nature of the angle of repose

The compatibility of AOR values measured (with the present method, see Figures 12 and 19) in both axisymmetric and plane strain configurations of the reference device could confirm a constitutive nature of the AOR inferred in, e.g., [5, 6, 7], suggesting to compare the latter with shear strength properties of the granular material. Generally speaking in solid-like granular mechanics, these shear strength properties may refer either to a critical state or a state of maximum stress ratio, the two being possibly different depending on initial porosity.

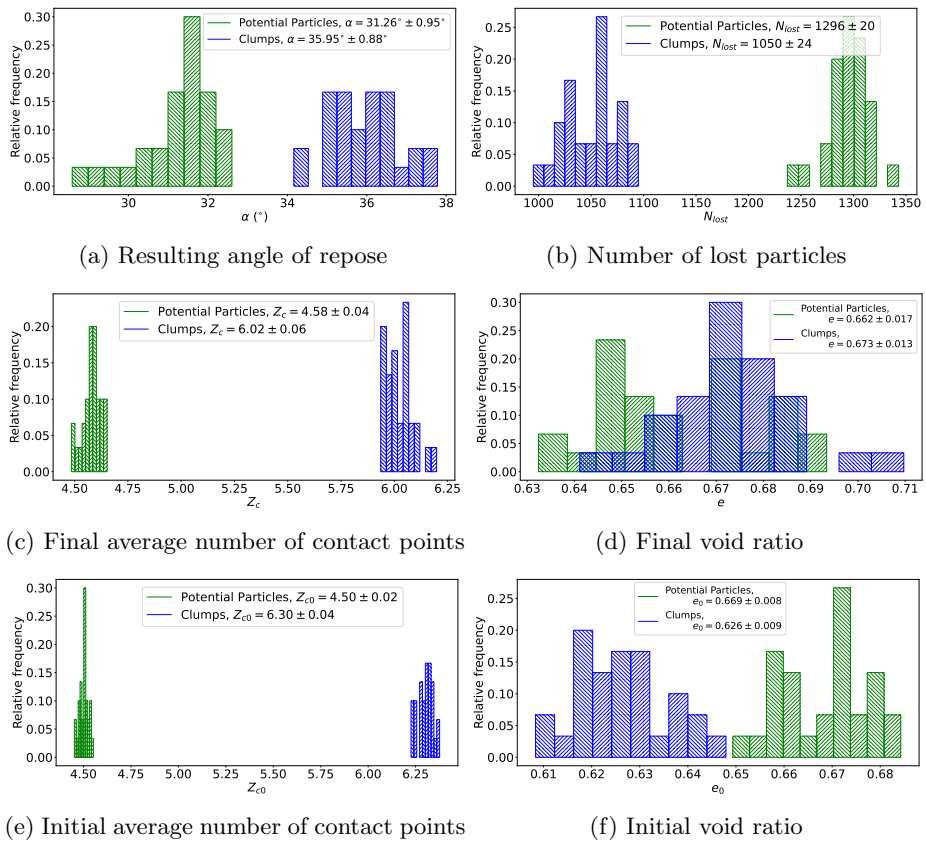

(a) Resulting angle of repose

(b) Number of lost particles

(c) Final average number of contact points

(d) Final void ratio

(e) Initial average number of contact points

(f) Initial void ratio

Fig. 20: Characterization of the PP-CLP series on particle concavity in terms of initial and final states

Here, it is first determined whether the AOR α evolves with respect to the initial void ratio e_0, which would contradict the definition of a critical state property. This is done by performing a "CLP4" series of simulations with the clump model using several samples at different initial porosities, whose parameters are given in Table 11. The initial void ratio e_0 is controlled by momentarily altering the inter-particle friction angle during the generation of the sample, φ_{gen}, whereby lower φ_{gen}-values lead to denser packings, as plotted in Figure 21 (a) where the error bars represent the standard deviation of e_0 on all 10 simulations performed at the same φ_{gen}. Figure 21 (b) shows α against e_0 and reveals some decreasing tendency of α for $e_0 < 0.55$ in both configurations that would be more consistent with an interpretation of the AOR in terms of a porosity-dependent maximum friction angle. However, the significant dispersion of the results prompts the need for further investigations in the following.

In addition, it is to note that a critical state interpretation of the repose would impose a correlation between critical state values of porosity (or void ratio) and mean pressure p in the form

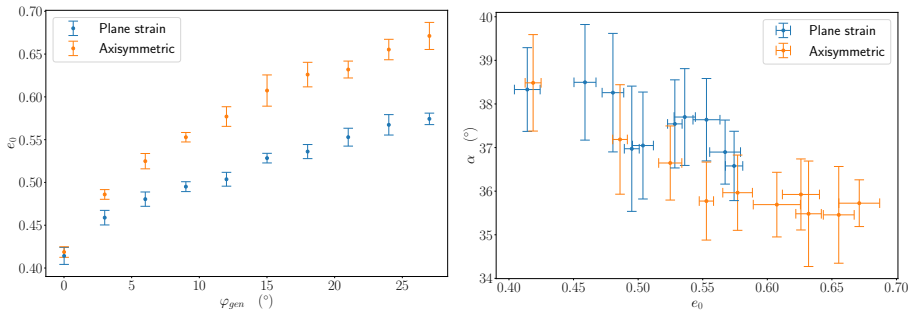

(a) Resulting e_0 against used φ_{gen} during packing preparation

(b) Angle of repose α against e_0

Fig. 21: Influence of the initial void ratio e_0 - CLP4 series

of a critical state line (CSL). Assuming, likewise to void ratio e, that an average (i.e. global) stress tensor is a meaningful quantity to characterize the heap in spite of gravity, the Appendix B recalls the expression of the latter tensor and the corresponding mean stress p in Equation B17. The final states (e, p) of a large set of 400 heaps simulated in the previous series CLP1, CLP4 together with a forthcoming CLP5 (grouped under a CLPX notation) are then compared in Figure 22 with the CSL of the present granular material, previously determined in [28] from DEM triaxial tests. The latter were performed in quasi-static conditions with a constant lateral stress in two directions and an imposed a strain rate in the third direction. Each of the 105 triaxial tests plotted on Figure 22 contained 7,500 clumps, which was shown to be enough to constitute a REV for the study of the material stress-strain behaviour. The critical state was observed to be attained when the axial strain ϵ_{ax} reaches 0.6, i.e. both the deviatoric stress and volumetric strain were unaffected by further deformations. Any critical state quantity is thus computed as an average of its value over $\epsilon_{ax} \in [0.6, 0.8]$. It is to note that it was shown in [28] to be more relevant to consider rattlers (particles having at most 1 contact) as voids when determining the CSL of a granular material, to avoid an unphysical increase of the CSL in the (e, p) plane for low p. This is especially important here since body weights are the only external forces present in the CLPX series, making the average mean stress possibly quite low (≈ 100 Pa), depending on mass density.

From the comparison in Figure 22, one can first note that the mechanical states in the CLPX series regroup around two different mean pressures: 126 ± 18 Pa and 1444 ± 471 Pa, in line with the two different values used for the particle density throughout the CLPX series. Whatever the mass density, the mean pressure in axisymmetric

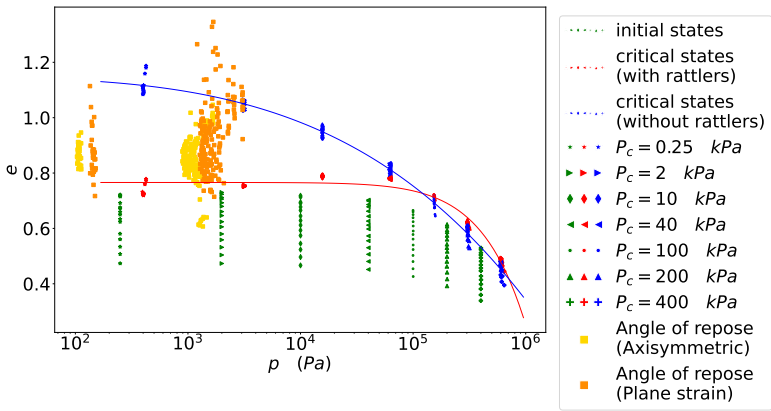

Fig. 22: Heaps' states after the collapse compared to the critical state line as determined in [28] from a large set of triaxial tests with different initial states in terms of void ratio and/or confining pressure P_c

heaps is lower than the mean pressure in plane strain heaps, and the dispersion in final void ratio is smaller. Most importantly, the heap states are clearly not consistent with the blue-colored (rattlers excluded) CSL serving as reference, which already suffices to exclude the assumption that a heap of particles under gravity is at critical state.

For completeness, the angle of repose of these CLPX series is still furthermore directly compared in Figure 23 with the critical state friction angle ϕ_{crit} and the (porosity;mean stress)-dependent peak friction angle ϕ_{peak} of the material, determined on the triaxial simulations from [28]. The AOR is therein shown to be significantly different (higher from approx. 10 degrees) than ϕ_{crit}. It actually lies in the observed interval for ϕ_{peak}, even though both are observed to be essentially different.

From the observations that the repose states are not consistent with the shear strength properties of the granular material, neither the critical one nor the maximum one, the AOR is concluded to bear no constitutive nature. Interpreting the repose stress state σ_{ij}^{glob} with its extreme principal stresses $\sigma_1^{glob} \geq \sigma_3^{glob}$ in terms of a mobilized friction angle ϕ_{mob}, given in Equation 36 using the soil mechanics sign convention:

$$\phi_{mob} = \arctan\left(\frac{\sigma_1^{glob} - \sigma_3^{glob}}{2\sqrt{\sigma_3^{glob}\sigma_1^{glob}}}\right) \qquad (36)$$

, no obvious correlation is actually found in Figure 24, no matter the shape model, between the mechanics of the heap, ϕ_{mob}, and its geometry, α, which would have been mandatory for a constitutive interpretation.

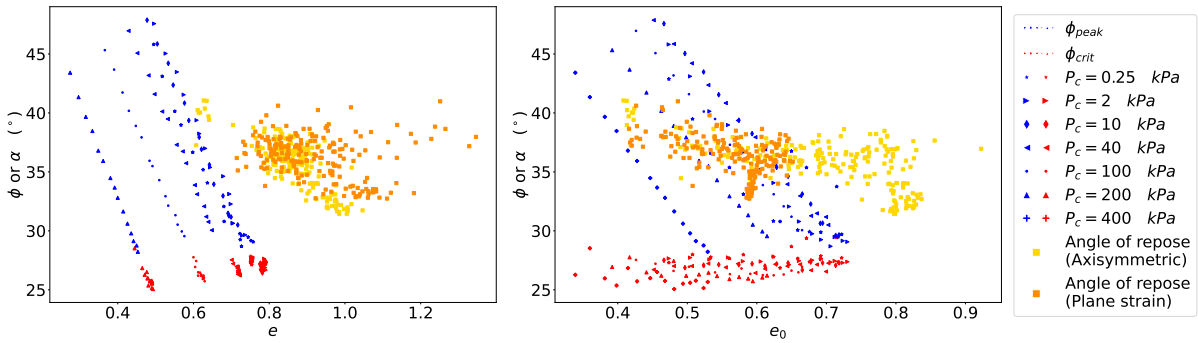

(a) With respect to e (b) With respect to e_0

Fig. 23: Angle of repose α and triaxial properties, ϕ_{crit} and ϕ_{peak}, with respect to void ratio (current, e, or initial, e_0)

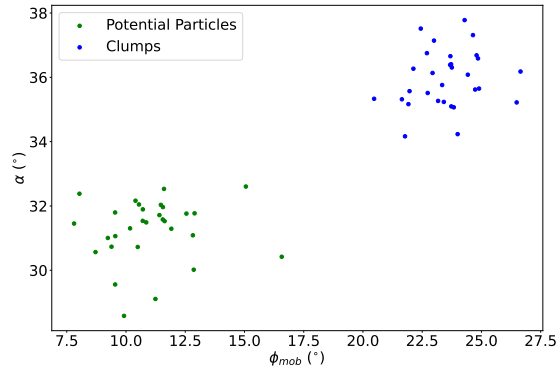

Fig. 24: Angle of repose α against mobilized friction angle ϕ_{mob} for heaps of the PP-CLP series.

4.5 Effect of the sample size on the angle of repose

Since the default number of particles in both configurations is low compared e.g. to the number of particles necessary to constitute a REV for the triaxial tests with rigid boundaries (7500 in [28, 29] for the same or another granular material), it is finally investigated to which extent the sample size can affect the present discussion, performing a last "CLP5" series that adopts the clump model and an evolving number of particles N_{part} (see Table 12 for all parameters). Doing so, the dimensions of the container are homothetically modified according to ${N_{part}}^{1/3}$, which insures to keep similar geometries (consistent length ratios between every 3 axes) when the total volume $V \propto N_{part}$ increases.

Figure 25 shows the AOR values obtained in this CLP5 series, with error bars from the standard deviation computed on the ten simulations performed for each value of N_{part}. An exponential model is proposed to fit the data and provide an extrapolated value of α for an infinite number of particles:

$$\alpha_{model}(N_{part}) = a + be^{cN_{part}} \qquad (37)$$

with a, b and c the three model parameters. Figure 25 (a) illustrates that the $N_{part} = 2,150$ case is the only one where the AOR values from both configurations are compatible with the idea of a common value. On Figure 25 (b) the horizontal

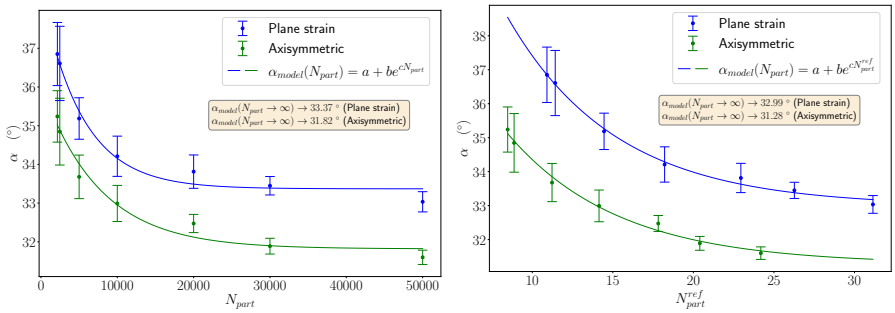

(a) α against N_{part} (b) α against N^{ref}_{part}

Fig. 25: Effect of the sample size on the angle of repose - CLP5 series

axis represents N^{ref}_{part}, the number of particle along one dimension of the base of the box:

$$N^{ref}_{part} = \left(\frac{N_{part}}{V_{box}}\right)^{\frac{1}{3}} L_\eta \tag{38}$$

with $V_{box} \in \{V_{cyl}, V_{par}\}$ and $L_\eta \in \{R_{cyl}, L_{par}\}$.

For bigger systems with a higher N_{part} a clear difference appears, with a negligible standard deviation. According to the exponential decay model, an asymptotic difference difference between the two configurations would be 1.19° which corresponds to approximately 3.59% of the measurement in the plane strain configuration.

The present dependency to N_{part} constitutes a last argument against the constitutive nature of the AOR, making fortuitous the near-similarity of α initially observed between the two configurations, in connection with the particular values of N_{part} used in the reference experiments.

5 Conclusion

In the framework of a round-robin activity providing an experimental reference, the angle of repose of a granular material has been studied with DEM, adopting two distinct characterizations for particle shape: concave clumps of spheres and convex-simplified potential particles, with a quantification of the morphological differences between the two (and the experimental reference), in terms e.g. of convexity and sphericity.

A methodological discussion has then been first proposed for generic angle of repose studies, designing systematic measurement procedures of the slope angle and of the void ratio of the heap, the latter being a possible factor of influence onto the former, as a fundamental property of granular matter.

Physically, a thorough analysis provided a number of consistent observations that the AOR measured on the considered devices does not

bear a constitutive nature but is instead process-dependent. In the comparison with experiments, while adopting a simpler measurement method of the AOR due to experimental limitations, the clump approach successfully predicted the AOR within a 8% tolerance. On the other hand, the potential particles underestimated to a greater extent the AOR, as expected due to their artificial convexity. Even though the material particles had a fairly high convexity value ($C = 0.954$), neglecting their local concavities brought down the AOR from $35.95 \pm 0.88°$ to $31.26 \pm 0.95°$.

It is interesting to note that both the clump and the potential particle shape descriptions share the same dimensions in terms of a minimal bounding box and thus the same flatness and elongation values, prompting the need for a systematic investigation of other particle-scale shape indices that would possibly affect the AOR.

Appendix A YADE implementations of visco-elasticity

With reference to the normal contact law in Equation 2 and for the clump approach (which use here the `Ip2_ViscElMat_ViscElMat_ViscElPhys` and `Law2_ScGeom_ViscElPhys_Basic` YADE classes), c_n is computed from a given normal restitution coefficient e_n according to the mass-dependent expression of [30], recalled in Equation A1:

$$e_n = \begin{cases} \exp\left[-\frac{\beta}{\omega}\left(\pi - \arctan\frac{2\beta\omega}{\omega^2-\beta^2}\right)\right] & \text{for } \beta < \frac{\omega_0}{\sqrt{2}} \\ \exp\left[-\frac{\beta}{\omega}\arctan\frac{2\beta\omega}{\omega^2-\beta^2}\right] & \text{for } \beta \in \left[\frac{\omega_0}{\sqrt{2}};\ \omega_0\right] \\ \exp\left[-\frac{\beta}{\Omega}\ln\frac{\beta+\Omega}{\beta-\Omega}\right] & \text{for } \beta > \omega_0 \end{cases} \tag{A1}$$

where $\beta = \frac{c_n}{2m}$, $\omega_0 = \sqrt{\frac{K_n}{m}}$, $\omega = \sqrt{{\omega_0}^2 - \beta^2}$ and $\Omega = \sqrt{\beta^2 - {\omega_0}^2}$, with m being the harmonic-average particle mass and K_n the normal contact stiffness. Equation A1 is solved inside YADE using a small number of Newton-Raphson iterations to make the inverse calculation of c_n based on the desired value of e_n. A straightforward calculation of c_n for the linear contact model has been provided in Equation (B4) of [31] via curve-fitting of the exact solution of [30], which is not however employed here.

For the potential particles approach (through, e.g., `Ip2_FrictMat_FrictMat_KnKsPhys` and `Law2_SCG_KnKsPhys_KnKsLaw` classes), a viscous damping parameter β_n serves as input for deriving c_n, consistently with a desired e_n and [32] via Equation A2:

$$\beta_n = -\frac{\ln e_n}{\sqrt{{\ln e_n}^2 + \pi^2}} \tag{A2}$$

Then, the viscous damping coefficient is calculated as in Equation A3:

$$c_n = 2\beta\sqrt{m \cdot K_n} \tag{A3}$$

Appendix B A global stress tensor accounting for gravity

In order to evaluate the stress state of the heap, one has to compute the stress tensor from the contact forces of all the contacts. Moreover, gravity being present in the simulations and at the origin of the movement, gravitational forces should thus be accounted for. In this subsection:

- $\mathbb{S}$ is the set containing all particles,
- $\mathbb{C}^{ext}$ is the set containing all the contacts between particles and boundaries,
- the upper-script $\cdot^p$ specifies that the quantity is taken for a particle p,
- the upper-script $\cdot^c$ specifies that the quantity is taken for a contact c,
- the sub-script $\cdot_{,x_i}$ denotes the derivative with respect to x_i,
- the total volume of the heap is noted V and can be determined from the volumes of all tetrahedrons V^{tet} given by the Delaunay triangulation on particles centers (see previous section 3.3.1): $V = \bigcup_{p\in\mathbb{S}} V^{tet}$,
- the number of underline denotes the order of a tensor ($\underline{\cdot}$ for vectors and $\underline{\underline{\cdot}}$ for matrices),
- the Kronecker symbol δ_{ij} and Einstein's notation will be used,
- classical sign convention for stress is adopted, where the traction vector $\underline{t} = \underline{\underline{\sigma}}.\underline{n}$ applies onto the system for an outwards normal $\underline{n}$.

The global stress tensor $\underline{\underline{\sigma}}^{glob}$ can be expressed according to the local stress tensor $\underline{\underline{\sigma}}$:

$$\underline{\underline{\sigma}}^{glob} = \frac{1}{V}\int_V \underline{\underline{\sigma}} dV \tag{B4}$$

One can compute $\underline{\underline{\sigma}}$ using the divergence of the third order tensor $\underline{\underline{\sigma}}\otimes\underline{x}$ (with $\underline{x}$ the position of any point in V with respect to a given, even though arbitrary, origin):

$$\left(\sigma_{ik}x_j\right)_{,k} = \sigma_{ik,k}x_j + \sigma_{ik}x_{j,k} \tag{B5}$$

Since the measurement is made when the heap is under equilibrium, the following equation holds, denoting $\underline{g}$ the gravitational acceleration and ρ the particle density:

$$\sigma_{ij,j} = -\rho g_i \tag{B6}$$

Moreover, $x_{j,k} = \delta_{jk}$, thus:

$$\sigma_{ik}x_{j,k} = \sigma_{ij} \tag{B7}$$

By replacing Equation B6 and Equation B7 in Equation B5 one gets:

$$\sigma_{ij} = (\sigma_{ik}x_j)_{,k} + \rho g_i x_j \tag{B8}$$

Equation B4 then gives:

$$\sigma_{ij}^{glob} = \frac{1}{V}\int_V \left((\sigma_{ik}x_j)_{,k} + \rho g_i x_j\right) dV \tag{B9}$$

$$= \frac{1}{V}\sum_{p\in\mathbb{S}} \int_{V^p} \left((\sigma_{ik}x_j)_{,k} + \rho g_i x_j\right) dV \tag{B10}$$

because $\sigma_{ij} \neq 0$ only on V^p

$$= \underbrace{\frac{1}{V}\sum_{p\in\mathbb{S}} \int_{V^p} (\sigma_{ik}x_j)_{,k}\, dV}_{\sigma_{ij}^C} + \underbrace{\frac{1}{V}\sum_{p\in\mathbb{S}} \int_{V^p} \rho g_i x_j dV}_{\sigma_{ij}^G} \tag{B11}$$

Particles having an homogeneous density, one furthermore has, with m^p and $\underline{x}^p$ the mass and center of p :

$$\int_{V^p} \rho x_j dV = m^p x_j^p \tag{B12}$$

The part of $\underline{\underline{\sigma}}$ due to gravity (σ_{ij}^G) can thus be written:

$$\sigma_{ij}^G = \frac{1}{V}\sum_{p\in\mathbb{S}} m^p g_i x_j^p \tag{B13}$$

As for the part due to contacts (σ_{ij}^C), Green-Ostrogradski theorem gives:

$$\sigma_{ij}^C = \frac{1}{V}\sum_{p\in\mathbb{S}} \int_{\partial V^p} \sigma_{ik}x_j n_k dS \tag{B14}$$

Considering the traction vector $\underline{t} = \underline{\underline{\sigma}}.\underline{n}$, one has:

$$\sigma_{ij}^C = \frac{1}{V}\sum_{p\in\mathbb{S}} \int_{\partial V^p} t_i x_j dS \tag{B15}$$

The traction vector is not nil only on contact points. Since the system is closed, contact forces between particles cancel each other leaving only forces comming from outside of V. As a consequence, one can only consider the contact forces between particles and walls. For these contacts f^c denotes the contact force exerted by the wall on the particle and x^c the contact point. One has:

$$\sigma_{ij}^C = \frac{1}{V}\sum_{c\in\mathbb{C}^{ext}} f_i^c x_j^c \tag{B16}$$

Finally, the global stress tensor for a stable heap of particles made of homogeneous particles and subjected to gravity is:

$$\sigma_{ij}^{glob} = \frac{1}{V}\sum_{c\in\mathbb{C}^{ext}} f_i^c x_j^c + \frac{1}{V}\sum_{p\in V} m^p g_i x_j^p \tag{B17}$$

The mean stress can then be computed as $p = \frac{\mathrm{Tr}(\underline{\underline{\sigma}}^{glob})}{3}$.

Appendix C Influence of the wall velocity

In both configurations a wall holding the particles moves in order to let them fall. The way particles fall depends on the velocity at which the wall

moves, but once the heap is stabilized the measurement of the AOR could be the same no matter the velocity. This could allow the increase of the wall velocity V_{wall} and thus the decrease of the time cost. To know the influence of V_{wall} on the AOR, a series of simulations, CLP3, is performed with the clump model. Its parameters are given in Table C1. For each value of the speed-up factor, 10 simulations are performed.

Figure C1 shows the results of the CLP3 series. The symbols correspond to the mean measurement over the 10 simulations performed with the same V_{wall} and the error bars represent the standard deviation. One can state that in the plane strain configuration V_{wall} does not have an effect on α. However, in the axisymmetric configuration, α decreases sharply in the transition zone $10 < V_{wall}/V_{wall}^{ref} < 100$. In the plane strain configuration, $V_{wall}/V_{wall}^{ref} = 10,000$ can thus be used, while one should restrict to $V_{wall}/V_{wall}^{ref} = 10$ in the axisymmetric configuration. Table C2 gives a summary of the value of V_{wall} used throughout all AOR simulations in this paper.

Data availability

All YADE scripts used to perform the PP-CLP series are available online at https://forgemia.inra.fr/sacha.duverger/aor_nc_aix.

Acknowledgements

We thank the Japanese Geotechnical Society for organizing the DEM round robin test that motivated this study. The efforts of Dr Shuji Moriguchi (Tohoku University) are in particular gratefully acknowledged. We also acknowledge the support from the French "Sud" region to the recent LS-ENROC project with an acquisition of a server machine that could accomodate the 980 simulations presented herein.

Compliance with Ethical Standards

The authors have no competing interests to declare that are relevant to the content of this article.

References

[1] Derek Geldart, EC Abdullah, A Hassanpour, LC Nwoke, and IJCP Wouters. Characterization of powder flowability using measurement of angle of repose. *China Particuology*, 4(3-4):104–107, 2006.

[2] Hamzah M Beakawi Al-Hashemi and Omar S Baghabra Al-Amoudi. A review on the angle of repose of granular materials. *Powder technology*, 330:397–417, 2018.

[3] Pascale C Rousé. Comparison of methods for the measurement of the angle of repose

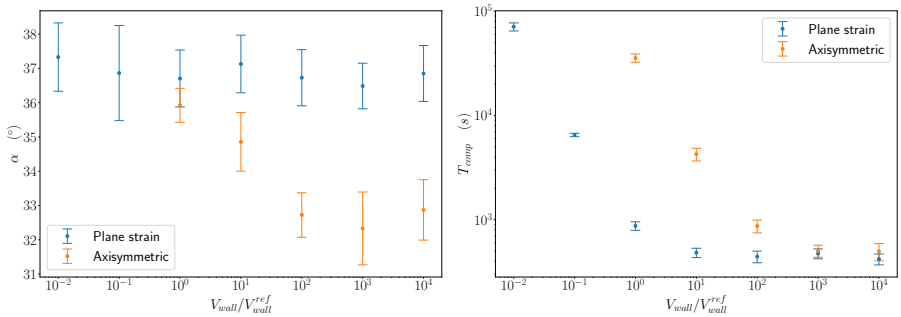

(a) Angle of repose (b) Time cost

Fig. C1: Wall velocity influence on the angle of repose and on the time cost - CLP3

of granular materials. *Geotechnical Testing Journal*, 37(1):164–168, 2014.

[4] Yukio Nakata, Shuji Moriguchi, Shintaro Kajiyama, Ryunosuke Kido, Naotaka Kikkawa, Hidetaka Saomoto, Daiki Takano, and Yosuke Higo. Experimental data of 3d printed granular material for verification of discrete element modeling simulation. *Soils and Foundations*, 62(4):101178, 2022.

[5] M. D. Bolton. The strength and dilatancy of sands. *Géotechnique*, 36(1):65–78, 1986.

[6] Michael Rackl and Kevin J. Hanley. A methodical calibration procedure for discrete element models. *Powder Technology*, 307:73–83, 2017.

[7] Thomas Roessler, Christian Richter, André Katterfeld, and Frank Will. Development of a standard calibration procedure for the dem parameters of cohesionless bulk materials – part i: Solving the problem of ambiguous parameter combinations. *Powder Technology*, 343:803 – 812, 2019.

[8] H.G. Matuttis, S. Luding, and H.J. Herrmann. Discrete element simulations of dense packings and heaps made of spherical and non-spherical particles. *Powder Technology*, 109(1):278–292, 2000.

[9] YC Zhou, BH Xu, AB Yu, and Paul Zulli. Numerical investigation of the angle of repose of monosized spheres. *Physical Review E*, 64(2):021301, 2001.

[10] Miki Y Matsuo, Daisuke Nishiura, and Hide Sakaguchi. Geometric effect of angle of repose revisited. *Granular Matter*, 16(4):441–447, 2014.

[11] Thorsten Pöschel and Volkhard Buchholtz. Static friction phenomena in granular materials: Coulomb law versus particle geometry. *Phys. Rev. Lett.*, 71:3963–3966, 1993.

[12] Hao Chen, Shiwei Zhao, and Xiaowen Zhou. Dem investigation of angle of repose for super-ellipsoidal particles. *Particuology*, 50:53–66, 2020.

[13] Nikola Topić, Jason AC Gallas, and Thorsten

Pöschel. Nonuniformities in the angle of repose and packing fraction of large heaps of particles. *Physical review letters*, 109(12):128001, 2012.

[14] Fathan Akbar, Elfi Yuliza, Nadya Amalia, Handika Dany Rahmayanti, and Mikrajuddin Abdullah. The slope of dry granular materials surface is generally curved. *Granular Matter*, 24(69), 2022.

[15] Hidetaka Saomoto, Naotaka Kikkawa, Shuji Moriguchi, Yukio Nakata, Masahide Otsubo, Vasileios Angelidakis, Yi Pik Cheng, Kevin Chew, Gabriele Chiaro, Jérôme Duriez, Sacha Duverger, Joaquín Irazábal González, Mingjing Jiang, Yohei Karasaki, Akiko Kono, Xintong Li, Zhuyuan Lin, Asen Liu, Sadegh Nadimi, Hitoshi Nakase, Daisuke Nishiura, Utsa Rashique, Hiroyuki Shimizu, Kumpei Tsuji, Takashi Watanabe, Xiaomin Xu, and Mourad Zeghal. Round robin test on angle of repose: Dem simulation results collected from 16 groups around the world. *Soils and Foundations*, 63(1):101272, 2023.

[16] V. Smilauer et al. *Yade Documentation 3rd ed.* The Yade Project, 2021. http://yade-dem.org/doc/.

[17] Vasileios Angelidakis, Sadegh Nadimi, Masahide Otsubo, and Stefano Utili. CLUMP: A Code Library to generate Universal Multi-sphere Particles. *SoftwareX*, 15:100735, 2021.

[18] Jean-Francois Ferellec and Glenn R McDowell. A method to model realistic particle shape and inertia in DEM. *Granular Matter*, 12(5):459–467, 2010.

[19] Guy Tinmouth Houlsby. Potential particles: a method for modelling non-circular particles in DEM. *Computers and Geotechnics*, 36(6):953 – 959, 2009.

[20] Chia Weng Boon, Guy Tinmouth Houlsby, and Stefano Utili. A new contact detection algorithm for three-dimensional non-spherical particles. *Powder Technology*, 248:94 – 102, 2013. Discrete Element Modelling.

[21] Reid Kawamoto, Edward Andò, Gioacchino Viggiani, and José E Andrade. Level set discrete element method for three-dimensional computations with triaxial case study. *Journal of the Mechanics and Physics of Solids*, 91:1–13, 2016.

[22] Jérôme Duriez and Cédric Galusinski. A level set-discrete element method in yade for numerical, micro-scale, geomechanics with refined grain shapes. *Computers & Geosciences*, 157:104936, 2021.

[23] Jérôme Duriez and Stéphane Bonelli. Precision and computational costs of Level Set-Discrete Element Method (LS-DEM) with respect to DEM. *Computers and Geotechnics*, 134:104033, 2021.

[24] Vasileios Angelidakis, Sadegh Nadimi, and Stefano Utili. SHape Analyser for Particle Engineering (SHAPE): Seamless characterisation and simplification of particle morphology from imaging data. *Computer Physics Communications*, 265:107983, 2021.

[25] Hakon Wadell. Volume, shape, and roundness of rock particles. *The Journal of Geology*, 40(5):443–451, 1932.

[26] Bruno Chareyre and Pascal Villard. Dynamic spar elements and discrete element methods in two dimensions for the modeling of soil-inclusion problems. *Journal of Engineering Mechanics*, 131(7):689–698, 2005.

[27] Claudio Rocchini and Paolo Cignoni. Generating random points in a tetrahedron. *Journal of graphics Tools*, 5(4):9–12, 2000.

[28] Sacha Duverger, Jérôme Duriez, Pierre Philippe, and Stéphane Bonelli. Rattlers' involvement for possibly looser critical states under higher mean stress. In *EPJ Web of Conferences*, volume 249, page 11002. EDP Sciences, 2021.

[29] T. Mohamed, J. Duriez, G. Veylon, and L. Peyras. DEM models using direct and indirect shape descriptions for Toyoura sand along monotonous loading paths. *Computers and Geotechnics*, 142:104551, 2022.

[30] Thomas Schwager and Thorsten Pöschel. Coefficient of restitution and linear–dashpot model revisited. *Granular Matter*, 9(6):465–469, 2007.

[31] Colin Thornton, Sharen J Cummins, and Paul W Cleary. An investigation of the comparative behaviour of alternative contact force models during inelastic collisions. *Powder technology*, 233:30–46, 2013.

[32] D Antypov and JA Elliott. On an analytical solution for the damped hertzian spring. *EPL (Europhysics Letters)*, 94(5):50004, 2011.

Table 11: Parameters used when investigating a possible influence of e_0 (CLP4 series, 200 simulations in total)

Configuration	N_{part}	ρ	e_0	Number of samples for each e_0
Plane strain	$2,150$	$10,000\ kg/m^3$	0.414 ± 0.010 0.459 ± 0.009 0.480 ± 0.008 0.495 ± 0.006 0.504 ± 0.008 0.528 ± 0.006 0.536 ± 0.008 0.553 ± 0.010 0.567 ± 0.012 0.574 ± 0.007	10
Axisymmetric	$2,468$		0.419 ± 0.006 0.486 ± 0.006 0.525 ± 0.009 0.553 ± 0.006 0.577 ± 0.011 0.607 ± 0.018 0.626 ± 0.014 0.632 ± 0.010 0.655 ± 0.012 0.671 ± 0.016	

Configuration	N_{part}	ρ	e_0	Number of samples
Plane strain	$2,150$	$10,000\ kg/m^3$	0.603 ± 0.010 0.604 ± 0.009 0.596 ± 0.005 0.596 ± 0.003 0.594 ± 0.002 0.591 ± 0.003 0.588 ± 0.001	10
	$2,468$			
	$5,000$			
	$10,000$			
	$20,000$		0.705 ± 0.011	
	$30,000$		0.693 ± 0.010	
	$50,000$		0.729 ± 0.017	
Axisymmetric			0.741 ± 0.006	
			0.758 ± 0.008	
			0.746 ± 0.016	
			0.736 ± 0.004	

Table 12: Parameters of heap simulations investigating the influence of N_{part} (CLP5 series, 140 simulations in total)

Configuration	N_{part}	ρ	V_{wall}/V^{ref}	e_0	Number of samples
Plane strain	$2,150$	$10,000\ kg/m^3$	10^i for $i \in [-2,4] \cap \mathbb{N}$	0.603 ± 0.010	10
Axisymmetric	$2,468$		10^i for $i \in [0,4] \cap \mathbb{N}$	0.693 ± 0.010	

Table C1: Parameters of heap simulations investigating V_{wall} influence (CLP3 series, 120 simulations in total)

Series	CLP1	CLP2	CLP4	CLP5	PP1	PP-CLP
V_{cyl}/V_{cyl}^{ref}	1	1	10	10	-	-
V_{par}/V_{par}^{ref}	1	1	10^4	10^4	10^3	10^3

Table C2: Wall velocity for all series of simulations